

Kubric: A scalable dataset generator

Klaus Greff¹ Francois Belletti¹ Lucas Beyer¹ Carl Doersch⁶ Yilun Du⁵

Daniel Duckworth¹ David J Fleet^{1,2} Dan Gnanapragasam¹ Florian Golemo^{4,9}

Charles Herrmann¹ Thomas Kipf¹ Abhijit Kundu¹ Dmitry Lagun¹ Issam Laradji^{3,9}

Hsueh-Ti (Derek) Liu² Henning Meyer¹ Yishu Miao¹⁰ Derek Nowrouzezahrai^{3,4}

Cengiz Oztireli^{1,8} Etienne Pot¹ Noha Radwan¹ Daniel Rebain^{1,7} Sara Sabour^{1,2}

Mehdi S. M. Sajjadi¹ Matan Sela¹ Vincent Sitzmann⁵ Austin Stone¹ Deqing Sun¹

Suhani Vora¹ Ziyu Wang¹⁰ Tianhao Wu⁸ Kwang Moo Yi⁷ Fangcheng Zhong⁸

Andrea Tagliasacchi^{1,2,11}

¹Google Research ²University of Toronto ³McGill University ⁴Mila ⁵MIT ⁶DeepMind

⁷UBC ⁸University of Cambridge ⁹ServiceNow ¹⁰Haiper ¹¹Simon Fraser University

Abstract

Data is the driving force of machine learning, with the amount and quality of training data often being more important for the performance of a system than architecture and training details. But collecting, processing and annotating real data at scale is difficult, expensive, and frequently raises additional privacy, fairness and legal concerns. Synthetic data is a powerful tool with the potential to address these shortcomings: 1) it is cheap 2) supports rich ground-truth annotations 3) offers full control over data and 4) can circumvent or mitigate problems regarding bias, privacy and licensing. Unfortunately, software tools for effective data generation are less mature than those for architecture design and training, which leads to fragmented generation efforts. To address these problems we introduce Kubric, an open-source Python framework that interfaces with PyBullet and Blender to generate photo-realistic scenes, with rich annotations, and seamlessly scales to large jobs distributed over thousands of machines, and generating TBs of data. We demonstrate the effectiveness of Kubric by presenting a series of 13 different generated datasets for tasks ranging from studying 3D NeRF models to optical flow estimation. We release Kubric, the used assets, all of the generation code, as well as the rendered datasets for reuse and modification.

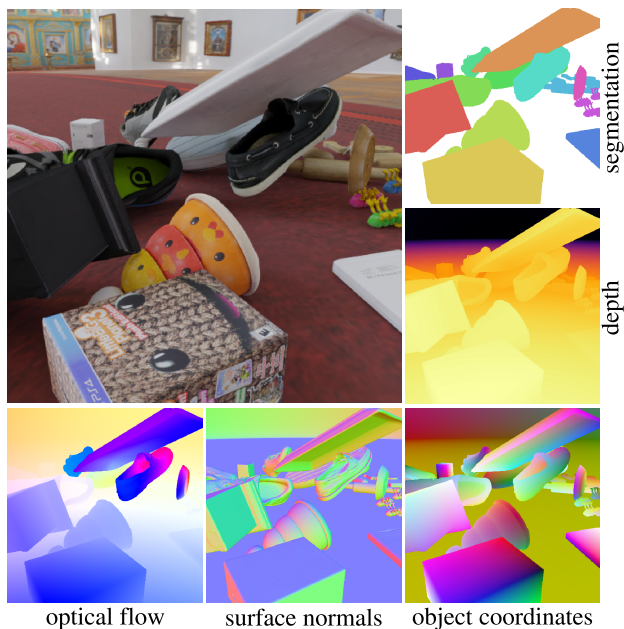


Figure 1. Example scene created and rendered with Kubric along with some of the automatically generated annotations.

1. Introduction

High quality data – at scale – is essential for deep learning. It is arguably as or more important than many architectural and training details. Nevertheless, even for many straightforward vision tasks, collecting and curating sufficient amounts

of data continues to be a daunting challenge. Some of the key barriers include the expense of high quality, detailed annotations, data diversity, control over task domain complexity, as well as concerns over privacy, fairness and licensing [4]. This paper advocates the use of synthetic data to circumvent many of these problems, for which we introduce Kubric, an open-source pipeline for generating realistic image and video data with rich ground truth annotations for myriad vision tasks.

Synthetic data has long been used for benchmark evaluation (e.g. for optical flow [6, 7]), as it supports rich ground-truth annotations, and fine-grained control over data complexity. It also enables systematic model evaluation under violations of model assumptions (e.g. rigidity). Synthetic data has also been used effectively for training. This includes seminal work on 3D human pose estimation from RGBD [85], and more recently on myriad tasks, including facial landmark detection [103], human pose from video [24], and semantic segmentation [116]. Photo-realism is often considered essential for narrowing the generalization gap, but even without perfect realism, synthetic data can be remarkably effective (e.g., flying chairs [26], MPI-Sintel [13] and more recently AutoFlow [89]).

Unfortunately, effective software tools for data generation are less mature than those for architecture design and training. It is therefore not surprising that most generation efforts, although costly, have been one-off and task specific. Although challenging to design and develop, what is needed is a general framework for photo-realistic generation that supports reuse, replication, and shared assets, all at scale, enabling workflows with large jobs concurrently on thousands of machines. Kubric addresses these issues with coherent framework, a simple Python API, and a full set of tools for generation at scale, integrating assets from multiple sources, with a common export data format for porting data into training pipelines, and with rich annotations for myriad vision tasks. In summary, our key contributions are:

- We introduce Kubric¹, a framework for generating photo-realistic synthetic datasets for myriad vision tasks, with fine-grain control over data complexity and rich ground truth annotations.
- Kubric enables generation at scale, seamlessly running large jobs over thousands of machines, generating TBs of data in a standard export data format.
- The versatility of Kubric is demonstrated by the creation of 13 datasets for new vision challenge problems, spanning 3D NeRF models to optical flow estimation, along with benchmark results.

2. Related Work

Synthetic data provides high quality labels for many image tasks such as semantic [16] and instance [102] segmentation, text localization [37], object detection [40], and classification [32]. There are many large synthetic datasets such as CLEVR [44], ScanNet [21], SceneNet RGB-D [65], NYU v2 [67], SYNTHIA [80], virtual KITTI [33], and flying things 3D [64] for specific tasks. However, these datasets rarely contain all possible annotations for all image tasks, lacking key signals such as camera pose, instance or semantic segmentation masks, or optical flow. This is particularly challenging for multi-task problems like co-training a neural scene model with semantic segmentation [118]. Moreover, fixed datasets can introduce biases [94, 95] such as an object-centric bias [71] and photographer’s bias [5]. By contrast, Kubric automatically generates the image cues for each frame and easily support a variety of viewing angles and lighting conditions.

Specialized Synthetic Data Pipelines. There are many hand-crafted pipelines for synthetic data generation [37, 49, 66] built off of rendering engines like Blender [9] and Unity3D [11]. While these pipelines mitigate biases in viewing angles and lighting, they are often specialized for a *particular* task. This makes it challenging to adapt them to provide additional annotations without in-depth knowledge of the underlying rendering engine. Real world to sim pipelines capture real-world data via 3D scans and then convert them into a synthetic data format. [56] creates high quality room scenes, but has many manual steps including pose alignment and material assignment. [27] also utilizes 3D scans, and provides control over a wide range of scene parameters, including camera position, field of view, and lighting, as well as a number of per frame image cues. While these approaches produce high quality data for a particular captured scene, the pipeline still relies on 3D scans of the full scene, which imposes a bottleneck for scaling.

| Name | Rendering | GI | Physics | Scaling | DL |
|-------------------|-----------|----|----------|---------|----|
| Playing4Data [78] | (Game) | × | (Game) | × | × |
| UnrealCV [75] | UE4 | × | UE4 | ✓ | × |
| TDW [34] | Unity | × | PhysX | ✓ | × |
| iGibson [106] | PyRender | × | PyBullet | ✓ | × |
| Habitat [91] | Magnum | × | Bullet | ✓ | × |
| OpenRooms [56] | OptiX | ✓ | – | × | × |
| Omnidata [27] | Blender | ✓ | – | × | ✓ |
| Blenderproc [23] | Blender | ✓ | Bullet | × | × |
| Kubric | Blender | ✓ | PyBullet | ✓ | ✓ |

Table 1. Rendering: Blender any OptiX are ray tracing engines, all others are based on rasterization; GI: support for global illumination; Physics: engine for physics simulation; Scaling: Easy to scale to very large datasets. DL: Data-loader integration with machine learning frameworks (PyTorch/TF).

¹<https://github.com/google-research/kubric>

Generic Dataset Creation Pipelines. General purpose synthetic data pipelines (like Kubric) aim to address these issues by supporting arbitrary random compositions of meshes, textures, pre-existing scenes, etc. from collections of 3D assets. This mitigates some of the scaling considerations of real world to sim pipelines and more easily supports composition of assets from different datasets. These pipelines differ along various dimensions (see Tab. 1). One important differences is the use of rendering engine, where ray-tracing engines support global illumination and other advanced lighting effects, which allow for a higher degree of realism than rasterization engines at the cost of a higher computational demand. Most general purpose synthetic data generation pipelines such as [53, 83, 84, 93, 106] are build on rasterization, which makes them very fast, often to the point of generating entire datasets on a single GPU machine. ThreeDWorld [34] is an excellent example for such an engine with a flexible Python API, comprehensive export capabilities to a Unity3D based rasterization engine, the NVidia Flex [61] physics simulator and even sound generation via PyImpact [96]. The framework closest in scope to Kubric is BlenderProc [23]: a ray-tracing based pipeline built on Blender, which supports the generation of high-quality renders and comprehensive annotations as well as rigid-body physics simulations. The main differences lie in Kubric’s focus on scaling workloads to many workers, and its integration with tensorflow datasets.

3. Infrastructure

Kubric is a high-level python library that acts as glue between: a rendering engine, a physics simulator, and data export infrastructure; see Figure 2. Its main contribution is to streamline the process and reduce the hurdle and friction for researchers that want to generate and share synthetic data.

3.1. Design Principles

Openness. Data-generation code should be freely usable by researchers both in academia and in industry. Kubric addresses this by being open-source with an Apache2 licence, and by only using software with similarly permissive licenses. Together with the use of free 3D assets and textures, this enables researchers to share not just the data, but also enable others to reproduce and modify it.

Ease of use. The fragmentation of computer graphics formats, conventions and interfaces is a major pain point for setting up and reusing data-generation code. Kubric minimizes this friction by offering a simple object-oriented API interface with PyBullet and Blender behind the scenes, hiding the complexities of setup, data transfer, and keeping them in sync. We also provide pre-processed 3D assets from a variety of data sources, that can be used with minimal effort.

Realism. To be maximally useful, a data-generator should

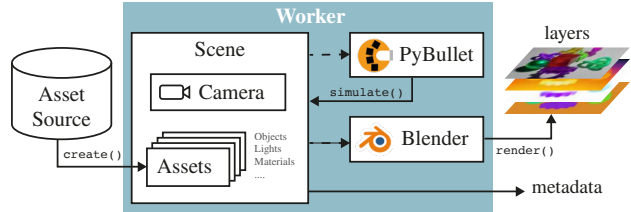


Figure 2. *Overview* – a typical Kubric worker randomly populates a scene with assets loaded from an external source, possibly runs a physics simulation, renders the resulting frames, and finally exports the images, annotation layers, and other metadata.

be able to model as much as possible of the structure and complexity of real data. The Cycles raytracing engine of Blender supports a high level of realism and can model complex visual phenomena such as reflection, refraction, indirect illumination, subsurface-scattering, motion-blur, depth of field, etc. Studying these effects is important, and they also help to reduce the generalization gap.

Scalability. Data generation workloads can range from simple toy-data prototyping all the way to generating massive amounts of high-resolution video data. To support this entire range of usecases, Kubric is designed to seamlessly scale from a local workflow to running large jobs on thousands of machines in the cloud.

Portable and Reproducible. To facilitate reuse of data-generation code, it is important that the pipeline is easy to setup and produces the same results — even when executed on different machines. This is especially important due to the difficulty in installing the Blender Python module [31] and the substantial variations between versions. By distributing a Kubric Docker image, we ensure portability and remove the bulk of the installation pain.

Data Export. Kubric by default exports a rich set of ground truth annotations from segmentation, optical flow, surface normals and depth maps, to object trajectories, collision events and camera parameters. We also introduce SunDs (see Sec. 3.4), a unified multi-task frontend for richly annotated scene-based data.

3.2. Kubric Worker – Figure 3

The typical Kubric workflow consists of writing a worker script that creates, simulates, and renders a single random scene. The full dataset is then generated by running this worker many times, and afterwards collecting the generated data. This division into independent scenes mirrors the i.i.d. structure of most datasets and supports scaling the generation process from local prototyping to a large number of parallel jobs; e.g. using the Google Cloud Platform (GCP), for which we provide convenience launcher scripts. We also plan to support an Apache Beam pipeline that combines generation, collection and post-processing of datasets into a single convenient (but ultimately harder to debug) workflow.

```

1 import numpy as np
2 import kubric as kb
3 asset_source = kb.AssetSource("/assets/KuBasic")
4 scene = kb.Scene(resolution=(640, 640))
5 renderer = kb.renderer.Blender(scene)
6 simulator = kb.simulator.PyBullet(scene)
7 # --- populate the scene
8 scene.camera = kb.PerspectiveCamera(position=(0, 5, 5),
9                                     look_at=(0, 0, 0))
10 scene += kb.Cube(name="floor", scale=(10, 10, .1),
11                position=(0, 0, -0.1), static=True)
12 scene += kb.PointLight(position=(-2.5, -1, 5), intensity=300)
13 rng = np.random.RandomState(seed=42)
14 for i in range(8): # place 8 random objects within a region
15     mat = kb.PrincipledBSDFMaterial(color=kb.random_hue_color(rng=rng),
16                                   metallic=rng.choice([0.0, 1.0]),
17                                   transmission=rng.choice([0.0, 1.0]))
18     obj = asset_source.create(rng.choice(asset_source.all_asset_ids),
19                              material=mat, velocity=rng.normal(size=3))
20     scene += obj
21     kb.move_until_no_overlap(obj, simulator, rng=rng,
22                             spawn_region=[[-1, -1, 0], [1, 1, 1]])
23 # --- execute the simulation, render, and save data to files
24 simulator.run()
25 renderer.save_state("output/scene.blend")
26 frames_dict = renderer.render()
27 kb.write_image_dict(frames_dict, "output")
28 kb.write_json({"camera": kb.get_camera_info(scene.camera),
29              "instances": kb.get_instance_info(scene)},
30             filename="output/metadata.json")

```

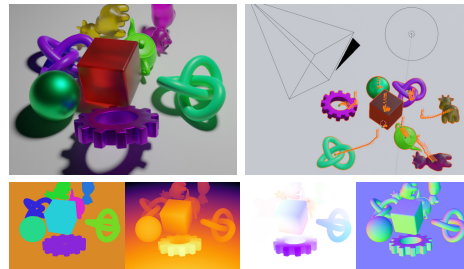


Figure 3. **Example worker** – A simple environment with a floor, a point light, a perspective camera and eight KuBasic objects placed without overlap (by rejection sampling) and a random velocity. The scene physics is then simulated by the PyBullet backend, and rendered by the Blender backend. Infinite random variations of the scene can be generated by varying the random seed (`rng`), and the result can be inspected in Blender by opening the `.blend` file *even before* rendering (top right). The exported image data includes annotations such as segmentation, depth, flow, and normals.

Scene structure. Each worker sets up a `Scene` object, which keeps track of global settings (e.g., resolution, number of frames to render, gravity), a `Camera`, and all the objects, including lights, materials, animations, etc., which we refer to collectively as `Assets`. They are the main abstractions used in Kubric to control the content of a scene, and they each expose a set of properties such as position, velocity or color. When an `Asset` instance is added to the scene, the corresponding objects are created in each of the `Views`. Currently this comprises the `PyBullet` simulator and the `Blender` renderer, but Kubric can be extended to support other views (e.g., the recently open-sourced `MuJoCo`). Kubric also maintains a link with the resulting data structure, and automatically communicates all changes to the properties of the assets to the connected views. That way, the user only has to work with the abstractions provided by Kubric, and does not have to worry about differences in interfaces or conventions.

Simulator. For physics simulation we interface with the open-source `PyBullet` physics engine [18] that is widely used in robotics (e.g., [43, 46, 107]). It can be used while populating the scene to ensure non-overlapping objects, but mainly it is used to run a (rigid-body) simulation, and to convert the resulting trajectories into keyframes and a list of collision events. `Bullet` can also handle rigged models, softbody simulations, and various constraints that Kubric does not yet support.

Renderer. Kubric uses the `bpy` module as an interface to Blender, a powerful open-source 3D computer graphics renderer which is widely used in game development and

for visual effects. Blender also comes with a powerful UI that can be used for interactively debugging and adjusting scenes, as well as creating and exporting new assets. For rendering we rely on `cycles` – Blender’s raytracing engine – which, unlike rasterized rendering engines, supports global illumination, accurately capturing effects such as soft shadows, reflection, refraction, and subsurface scattering. These effects are crucial for visual realism, and together with the vast set of other features of Blender, they enable artists to create photo-realistic 3D objects and scenes. The downside is that `cycles` can be several orders of magnitude slower than a rasterized rendering engine, but for Kubric we decided that this computational cost is a worthwhile tradeoff in exchange for the added realism and the ability to systematically study complex visual effects.

Annotations. Another important feature of Blender is the use of specialized render passes that compute auxiliary ground truth information. We leverage this feature to export (in addition to the RGB image) ① depth maps, ② instance segmentation, ③ optical flow, ④ surface normals, and ⑤ object coordinates (see Fig. 1). In addition to these image space annotations, Kubric also automatically collects object-centric metadata, such as 2D/3D trajectories, 2D/3D bounding boxes, velocities, mass, friction, camera parameters, collision events, as well as custom metadata.

3.3. Assets

A limiting factor in the creation of synthetic scenes is the availability of high-quality 3D assets. Several asset collections exist, but their use often requires substantial

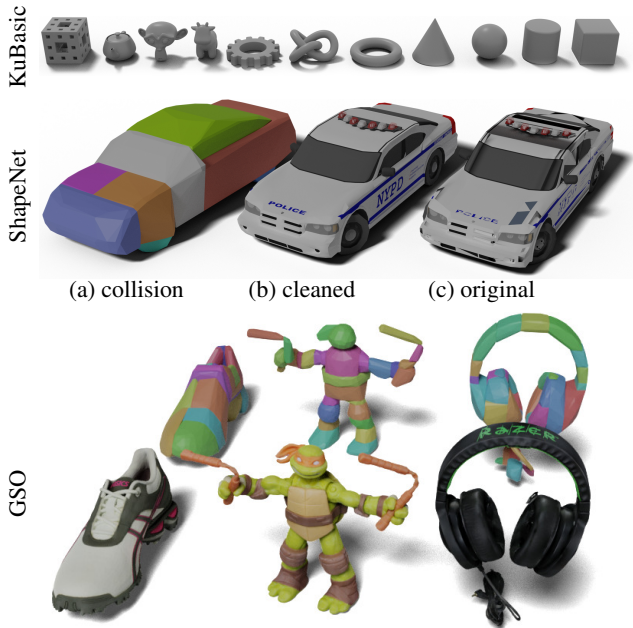


Figure 4. (top) The KuBasic assets collection. (middle) ShapeNet objects by default do not render well in Blender (c) due to problems with auto-smoothing and the lack of backface culling in cycles. (b) We processed all ShapeNet objects to fix these issues and (a) generated a collision mesh by first making the model watertight and then performing an approximate convex decomposition using VHACD. (bottom) Example assets from the Google Scanned Objects (GSO) dataset along with the generated collision meshes.

cleanup and conversion to make them compatible with a given pipeline. Kubric provides several preprocessed collections of assets in a public Google Cloud bucket. Using these assets is as simple as changing the path of the asset source with `kb.AssetSource(path)`. At the core level, each dataset source is associated with a `manifest.json` file storing high level aggregated information, without the need to traverse the entire folder structure. The "id" property of each entry in the manifest is in one-to-one correspondence to an archive file containing the data for the asset. Each of these archives contains a JSON-file with detailed metadata for a particular objects, including the paths to the sub-assets for rendering, collision detection, and the definition of physical properties in the Unified Robot Description Format (URDF) used by PyBullet. For textured models, we employ the GLTF standard [79], and store textures in binary format together with the geometry.

KuBasic. For simple prototyping we ship a small collection of eleven simple assets depicted in the top row of Fig. 4.

ShapeNetCore.v2. This dataset is a subset of the full ShapeNet dataset [14] with 51,300 unique 3D models from 55 with canonical alignment and common object categories annotations (both manually verified). Extensive pre-processing was performed to simplify the integration

of these assets within Kubric. These conversion scripts are available in the `shapenet2kubric` sub-directory; the conversion process can be easily reproduced by the Docker container available therein. This conversion process took ≈ 16 hours on a 80 core virtual machine (Google Cloud VM `n2-highcpu-80`) and parallelization across threads executed by Python’s `multiprocessing` library. A small set of models failed to convert (e.g., they had missing textures, erroneous materials, or simply crashed the conversion process) and are listed in the conversion code.

While many of the models within the dataset produce satisfactory renderings when visualized through OpenGL, rendering quality is significantly higher when a *photorealistic* renderer is employed (i.e., Blender Cycles). We collected the community’s wisdom (i.e., ShapeNet and Blender official forums) on how to tweak models to minimize the occurrence of visual artifacts. The conversion procedure is automated via scripted Blender modifiers and involves removing doubles, disabling auto-smoothing, splitting sharp edges, and infinitesimally displacing the faces of polygonal meshes along the primitive’s local normal. For the collision geometry, we first converted the assets into watertight meshes with ManifoldPlus [41], and then resorted to the VAHCD [62] implementation wrapped within PyBullet [19] to compute the convex decomposition of a 3D object, whose mass and inertia tensors were finally estimated by trimesh [22].

Google Scanned Objects (GSO) [77]. Is a dataset of common household objects that have been 3D scanned for use in robotic simulation and synthetic perception research. It is licensed under the CC-BY 4.0 License and contains $\approx 1k$ high-quality textured meshes; see Fig. 4. We publish pre-processed version of this dataset in the Kubric format, which again includes generated collision meshes.

Polyhaven [115]. is a public (CC0 licensed) library from which we have collected and pre-processed HDRI images for use as backgrounds and lighting, and textures for use in high-quality materials.

3.4. Scene Understanding Datasets (SunDs)

To facilitate ingesting data into machine learning models, we introduce, alongside Kubric, the SunDs (Scene Understanding Datasets) dataset front-end². SunDs is an API to access public scene understanding datasets. The field names and structure, shape, dtype are standardized across datasets. This allow to trivially switch between datasets (e.g. switch from synthetic to real data). All SunDs datasets are composed of two sub-datasets:

- The scenes dataset contains high level scene metadata (e.g., scene boundaries, mesh of the full scene, etc.).

²<https://github.com/google-research/sunds>

| Section | task domain | task domain | | | | | | | | | | | scale | | | | | |
|---------|----------------------|-------------|--------------|-------|----------------|-----------------|--------------|------------------|-------------------|-------------------|------------------|---------------|-------|-------------|--------------------|-------------|---|----|
| | | flow | segmentation | depth | camera 3D pose | object 3D poses | physics sim. | rigged animation | control backgrnd. | control materials | control lighting | new challenge | | sim-to-real | hypothesis testing | PII / legal | | |
| 4.1 | Object discovery | 2D | ✓ | ✓ | × | × | × | × | ✓ | × | ✓ | ✓ | ✓ | ✓ | × | × | × | TB |
| 4.2 | Optical flow | 2D | ✓ | × | × | × | × | × | ✓ | × | ✓ | × | ✓ | × | × | × | × | TB |
| 4.3 | NeRF & Texture | 3D | × | × | ✓ | × | × | × | × | × | × | × | × | × | × | × | × | MB |
| 4.4 | Pose-estimation | 2D | × | × | × | × | × | × | × | ✓ | ✓ | ✓ | ✓ | × | × | × | × | GB |
| 4.5 | Pre-training | 2D | × | × | × | × | × | × | × | × | × | × | × | × | × | × | × | GB |
| 4.6 | Robust NeRF | 3D | × | × | × | × | × | × | × | × | × | × | × | × | × | × | × | MB |
| 4.7 | Multi-view SOD | 2D | × | × | × | × | × | × | × | × | × | × | × | × | × | × | × | GB |
| 4.8 | Complex BRDFs | 3D | × | × | × | × | × | × | × | × | × | × | × | × | × | × | × | GB |
| 4.9 | 3D reconstruction | 3D | × | × | × | × | × | × | × | × | × | × | × | × | × | × | × | GB |
| 4.10 | Robust 3D recons. | 3D | ✓ | ✓ | × | × | × | × | × | × | × | × | × | × | × | × | × | MB |
| 4.11 | Point tracking | 2D | × | × | ✓ | ✓ | ✓ | ✓ | ✓ | × | × | × | × | × | × | × | × | TB |
| 4.12 | ToyBox | 3D | × | × | × | × | × | × | × | × | × | × | × | × | × | × | × | GB |
| 4.13 | Novel View Synthesis | 3D | × | × | × | × | × | × | × | × | × | × | × | × | × | × | × | GB |

Table 2. Overview of the datasets / challenges presented in Sec. 4.

- The frames dataset contains the individual examples within a scene (e.g., RGB image, bounding boxes, etc.).

SunDs abstracts away the dataset-specific file format (json, npz, folder structure, ...), and returns tensors directly ingestible by machine learning models (TF, Jax, Torch). Internally, SunDs is a wrapper around TFDS, which allows one to scale to huge datasets (\approx TB), to provide native compatibility with distributed cloud file systems (e.g. GCS, S3), and to leverage `tf.data` pipeline capabilities (prefetching, multi-threading, auto-caching, transformations, etc.).

To simplify even further data ingestion, SunDs introduce, on top of TFDS, the concept of tasks. Each SunDs dataset can be loaded for different tasks. Tasks control:

- Which features of the dataset to use/decode. Indeed, scene understanding datasets often have many fields (lidar, optical flow, ...), but only a small subset are used for any given task. Selecting which fields are used avoids the cost of decoding unnecessary features.
- Which transformation to apply to the pipeline. For example, the NeRF task will dynamically generate the rays origin/directions from the camera intrinsics/extrinsics contained in the dataset.

4. Kubric Datasets and Challenges

To demonstrate the power and versatility of Kubric, we next describe a series of new challenge problems, each with data³ generated by Kubric (see Tab. 2). They cover 2D and 3D tasks at different scales, with dataset sizes ranging from MBs to TBs. Each relies on a different subset of annotations (flow, segmentation, depth, camera pose, or object pose), makes use of a different subset of features (e.g., physics or rigged animation), and requires control over different factors (background, materials, or lighting). Any one dataset might have been generated by a simpler, specialized code-base, but

³The presented datasets along with the corresponding worker scripts can be found at <https://github.com/google-research/kubric>.

| Method | MOVi-A | MOVi-B | MOVi-C | MOVi-D | MOVi-E |
|-------------|----------------|----------------|----------------|----------------|----------------|
| SAVi [50] | 82.0 \pm 0.3 | 61.5 \pm 0.3 | 47.0 \pm 0.3 | 19.4 \pm 8.0 | 2.7 \pm 0.5 |
| SIMONE [45] | 61.8 \pm 2.0 | 30.7 \pm 3.3 | 19.8 \pm 0.5 | 34.1 \pm 0.7 | 34.9 \pm 0.6 |
| SAVi + BBox | 95.3 \pm 0.2 | 85.5 \pm 0.2 | 73.5 \pm 0.3 | 9.9 \pm 1.4 | 7.5 \pm 1.0 |

Table 3. **Object discovery** – Object segmentation performance, measured in terms of foreground ARI [36, 42] (FG-ARI \uparrow) in %. We compare two recent state-of-the-art models, SAVi [50] (trained using optical flow) and SIMONE [45]. SAVi + BBox additionally receives object bounding boxes as cues in the first frame.

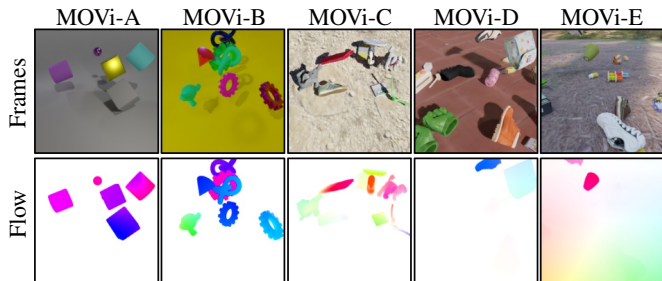


Figure 5. **Object discovery** – Dataset samples of MOVi of increasing visual complexity. MOVi-A uses objects inspired by CLEVR [44]. MOVi-B introduces additional primitive object types and colors. MOVi-C introduces real-world backgrounds and scanned 3D objects. MOVi-A to -C contain scenes of up to 10 moving objects (24 frames per video). MOVi-D & MOVi-E scenes have up to 23 objects, with only a small fraction of moving objects. In MOVi-E, the camera is moving in random directions.

this would have been extremely inefficient. Rather, with the versatility of Kubric, it was straightforward to create, extend and combine datasets, leveraging a common platform and shared engineering efforts.

These different challenges also highlight different uses of synthetic data. Some serve as benchmarks for comparing existing and future methods, while others provide additional training data for real-world applications (sim-to-real). Some are designed to empirically test specific hypotheses (e.g., in testing), while some focus on data that can be shared without privacy and legal concerns.

We describe 13 challenges in sections below; i.e., 4.6) Nerf reconstruction in the presence of non-static scenes structure; 4.7) a novel multi-view version of the salient object detection task; 4.8) a 3D reconstruction benchmark focussed non-Lambertian surfaces; 4.9) a study on scaling and generalization of SOFTRAS for reconstructing 3D meshes from a single image; 4.10) a study on the robustness of video-based reconstruction of 3D meshes with respect to mesh deformations and inaccurate flow; 4.11) a long-term dense 2D point tracking task including a novel contrastive tracking algorithm; 4.12) a large-scale multi-view semantic scene understanding benchmark; and 4.13) a challenging new-scene novel view synthesis dataset.

| Dataset | Parameters | Sintel | | KITTI-15 | |
|-------------------|------------|-------------|-------------|-------------|--------------|
| | | Clean | Final | AEPE | ER% |
| FlyingChairs (2D) | Manual | 2.27 | 3.76 | 7.63 | 38.5% |
| Kubric (3D) | Manual | 1.89 | 3.02 | 4.82 | 16.9% |
| AutoFlow (2D) | Learned | 2.08 | 2.75 | 4.66 | 15.3% |

Table 4. **Optical flow** – Comparison of pre-training RAFT on different optical flow datasets (lower is better for all metrics).

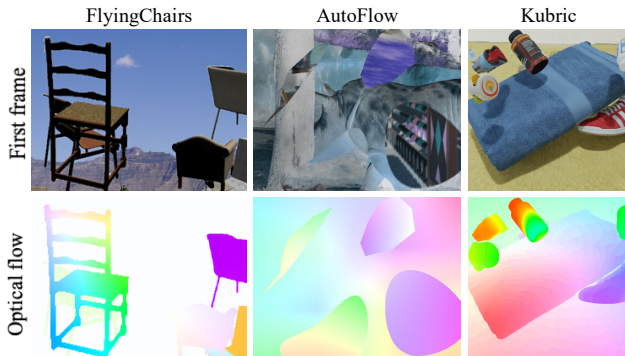


Figure 6. **Optical flow** – Chairs in FlyingChairs undergo 2D affine motion; random polygons in AutoFlow undergo nonrigid 2D motion; 3D objects in Kubric undergo 3D rigid-body motion.

4.1. Object discovery from video

Object discovery methods aim to decompose a scene into its constituent components and find object instance segmentation masks with minimal supervision. While recent models such as IODINE [36], MONet [12], GENESIS [28], and Slot Attention [59] succeed at decomposing simple scenes with uniform textures, decomposing dynamic scenes (i.e., videos) with high visual complexity and complex dynamics remains difficult. This challenge introduces five Multi-Object Video (MOVi) datasets, MOVi-A to -E (see Fig. 5), of increasing visual and dynamical complexity, aimed at testing the limits of existing object discovery approaches, enabling progress towards more realistic and diverse visual scenes.

We test two recent state-of-the-art video object discovery methods, SAVi [50] and SIMONE [45], for their ability to decompose videos into temporally consistent object segmentation masks (see Table 3). SAVi, which uses optical flow during training, performs better at decomposing videos with moving objects only, especially when receiving additional cues in the first frame of the video. Both methods decline in performance as complexity increases with an exception for static objects in MOVi-D and -E, which are sometimes partially captured by SIMONE. Neither method can reliably decompose scenes in all five datasets.

4.2. Optical flow

Optical flow refers to the 2D motion from pixels in one frame to the next in a video. It is fundamental to video processing and analysis. Unlike high-level vision tasks, we cannot obtain reliable, ground-truth optical flow on generic

| Frequency Cutoff | $10^{-0.5}$ | 10^0 | $10^{0.5}$ | 10^1 | 10^2 |
|-----------------------------|-------------|--------|------------|--------|--------------|
| PSNR \uparrow | 28.1 | 27.8 | 26.7 | 23.6 | 23.4 |
| Depth Variance \downarrow | 0.026 | 0.024 | 0.023 | 0.023 | 0.022 |

Table 5. **Texture-structure in NeRF** – Reconstruction error and depth variance for different texture frequency bands with NeRF on textured surface. Accuracy of color prediction improves as frequency of the texture becomes lower, while accuracy of the surface geometry degrades.

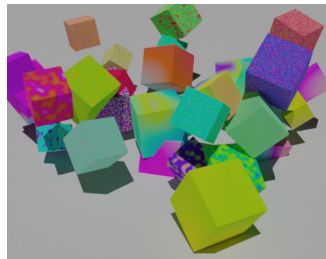


Figure 7. A NeRF dataset with procedural texture allows each pixel to be annotated with frequency information. This enables analysis of the frequency-structure relationship in the learned NeRF model.

real-world videos, even with human annotation. Optical flow is actually the first sub-field of computer vision to rely on synthetic data for evaluation [7].

Recent deep models, PWC-net [90], RAFT [92], and VCN [110], all rely on synthetic data for pre-training, like FlyingChairs [26]. However, FlyingChairs lacks photo-realism, uses synthetic chairs as the only foreground objects, and does not have general 3D motion. AutoFlow [89] learns rendering hyperparameters for generating a synthetic flow datasets, yielding large performance gains over FlyingChairs [89]. But AutoFlow adopts a simple 2D layered model, lacks 3D motion and realism in rendering. Our Kubric dataset addresses these shortcomings, as shown in Fig. 6.

We compare training RAFT on different datasets using the same training protocol [88, 89, 92]. As shown in Table 4, Kubric leads to significantly more accurate results than FlyingChairs when both use manually selected rendering hyperparameters, demonstrating the benefit of using 3D rendering. Kubric also performs competitively against AutoFlow. Note that this is not an apples-to-apples comparison, because the hyperparameters of AutoFlow have been learned to optimize the performance on the Sintel dataset [89]. These results suggest that learning hyperparameters for Kubric is likely to result in significant performance gains.

4.3. Texture-structure in NeRF

Neural radiance fields are inherently *volumetric* representations, but are commonly used to model the surfaces of solid objects. These NeRF surface models are a result of the model trying satisfy a multi-view reconstruction problem: to reconstruct surface detail consistently from multiple views, those details must lie in a thin slice of the volume around the true surface. Note that not all surfaces will encourage NeRF to build a surface model. Surfaces with flat color may still be

| Train data set | COCO + Active | COCO + Active + Synth |
|----------------|---------------|-----------------------|
| COCO [57] | 0.554 | 0.557 |
| Active [98] | 0.650 | 0.662 |
| Yoga | 0.391 | 0.427 |

Table 6. **Pose estimation** – results are improved out-of-domain by the addition of synthetic images of human models featuring poses outside the COCO domain; Keypoint Mean Average Precision (mAP) metric (higher is better)

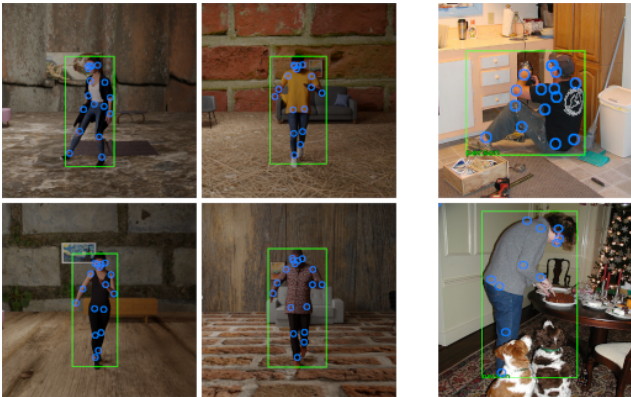


Figure 8. **Pose estimation** – fully annotated images from synthetic videos aimed at diversifying poses (left), motions, subjects and backgrounds featured in real-world annotated data sets, and (right) examples of COCO-equivalent images.

reconstructed as a non-solid volume. Hence, benchmarking NeRF methods according to how well they stay true to the actual surface depending on texture is an interesting aspect that is still unexplored.

To quantify this, we created synthetic scene containing flat surfaces, the textures of which are procedurally generated with blue noise to have varying spatial frequency. We annotate each pixel with the cutoff frequency of its texture and analyze the correlation between frequency, depth variance, and reconstruction error. We then train a NeRF model with this synthetic data. As shown in Table 5, we find that increasing frequencies are associated with lower depth variance, indicating better approximations to a hard surface, while also increasing the reconstruction error, showing that the network is less able to approximate the complex textures. It would be interesting to see how well future volumetric multi-view reconstruction methods would cope with this ambiguity and encourage hard surface boundaries.

4.4. Pose estimation

Pose-estimation-based interactive experience (e.g., Kinect) often feature human poses that remain under-represented in most data sets comprising user-generated pictures (e.g. COCO [57]), as picture-worthy poses present an obvious sampling bias. Simulated data can supplement real data with less aesthetic poses which are nonetheless

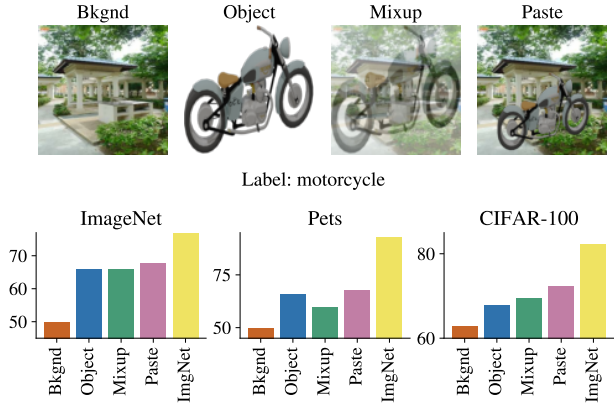


Figure 9. **Pre-training** a ResNet50 on synthetic Kubric data (top) and transferring it to standard benchmarks (bottom) halves the gap between random pre-training (Bkgnd) and ImageNet pre-training.

common in real-life human motions. Here we improve MoveNet [98], a CenterNet [119] based pose inference CNN usually trained on COCO [57] and Active [98] (a proprietary data set with more diverse poses). As in Simpose [120], training batches mix real and synthetic data with an 80/20% mixture. Unlike [120], synthetics do not provide additional labels (e.g., surface normals) but only contribute more diverse examples. As illustrated in Figure 8, the samples feature 41 rigged RenderPeople models placed in a randomized indoor scene where background elements and textures come from BlenderKit and TextureHeaven. Human poses are extracted from dancing and workout ActorCore animations. While licensing terms of non-CC0 assets forbid data publication, the data set can be re-generated with our open source software by any owner of the same mesh and animation assets. Synthetic data improves keypoint Mean-Average-Precision (see Table 6), in domain (on COCO and Active), and out-of-domain (on Yoga, a test set of contorted poses comprising 1000 examples). Synthetic data are therefore now routinely used in our human-centric training procedures for still images as well as videos.

4.5. Pre-training visual representations

Ever since AlexNet [55], the entire field of computer vision has benefited immensely from re-using “backbones” pre-trained on large amounts of data [25,52,54,76]. However, recent work casts doubt on the continued use of datasets that consist of vast collections of photos from the internet [8,112]. One potential way forward, which completely circumvents the downsides of web-image based data, is to use rendered data. This has recently shown great success for face recognition [103], and we hypothesize that synthetic data could also eventually replace web images for pre-training general computer vision backbones. In order to evaluate the promise of such a setting, we perform a small pilot experiment. Kubric was used to render ShapeNet objects in various random poses

| | easy | | | hard | | |
|-----------------------------|-----------------|-------|--------|-----------------|-------|--------|
| | maxF $_{\beta}$ | MAE | S $_m$ | maxF $_{\beta}$ | MAE | S $_m$ |
| Pre-trained | | | | | | |
| SINet [30] | 0.494 | 0.097 | 0.597 | 0.401 | 0.093 | 0.568 |
| EGNet [117] | 0.652 | 0.090 | 0.753 | 0.462 | 0.133 | 0.641 |
| BASNet [74] | 0.822 | 0.034 | 0.878 | 0.581 | 0.086 | 0.730 |
| CPD [105] | 0.811 | 0.029 | 0.872 | 0.594 | 0.068 | 0.742 |
| U ² -Net [73] | 0.825 | 0.032 | 0.882 | 0.594 | 0.083 | 0.743 |
| Fine-tuned | | | | | | |
| CPD [105] | 0.958 | 0.007 | 0.968 | 0.901 | 0.015 | 0.925 |
| U ² -Net [73] | 0.975 | 0.006 | 0.977 | 0.909 | 0.015 | 0.931 |
| Trained from scratch | | | | | | |
| CPD [105] | 0.957 | 0.008 | 0.967 | 0.906 | 0.015 | 0.928 |
| U ² -Net [73] | 0.967 | 0.009 | 0.971 | 0.890 | 0.021 | 0.916 |

Table 8. **Salient Object Detection** – Quantitative results as evaluated by max F-measure with $\beta^2 = 0.3$ [1], Mean Absolute Error [10] and Structure measure [29].

on transparent backgrounds. We pre-train a ResNet-50 to predict the object’s category from images that combine the object with a random background image in various ways, as shown in Fig. 9 (top). We then transfer this pre-trained model to various datasets, following the protocol in [52]. Figure 9 (bottom) shows that this simple pilot experiment already halves the gap between random pre-training and pre-training on ImageNet, suggesting that this is a promising approach.

4.6. Robust NeRF

Neural Radiance Fields [66] or NeRF, trains a representation of a static 3D scene via volume rendering by minimizing a photometric reconstruction loss of the form $\mathcal{L}(\theta) = \mathbb{E}_r \|I(r) - I_{\theta}(r)\|_2^2$, where r are rays corresponding to pixels of a multi-camera system. The nature of this loss implies that when the scene is *not perfectly static* across views, the recovered representation is corrupted; see Figure 11 (center). This challenge demonstrates that further research is still needed to fully address this problem; see Table 7. In the “teleport” challenge, while most of the scene remains rigid, we add impostor non-static object (i.e. the monkey head) randomly within the scene bounds, while in the “jitter” challenge the impostor position jitters around a fixed position. In other words, the two datasets evaluate the sensitivity of unstructured (teleport) vs. structured (jitter) outliers in the training process. Figure 10 showcases some of the training frames for each challenge. As shown in Table 7, while unstructured outliers are to *some degree* addressed by NeRF-L1 (−2.4 dB), structured outliers are significantly more challenging to overcome.

4.7. Multi-view object matting

Salient Object Detection (SOD) aims to segment out the most salient object in an image from the background.

| | static | teleport | jitter |
|---------|---------|----------|---------|
| NeRF-L2 | 43.5 dB | 25.5 dB | 27.4 dB |
| NeRF-L1 | 42.8 dB | 40.4 dB | 37.1 dB |

Table 7. **Robust NeRF** – Performance in PSNR $_{\uparrow}$ of classical NeRF-L2 [66] and its L1-robust version [113]. Note the performance is evaluated on test views (i.e. novel view synthesis) and *without* any impostors present.

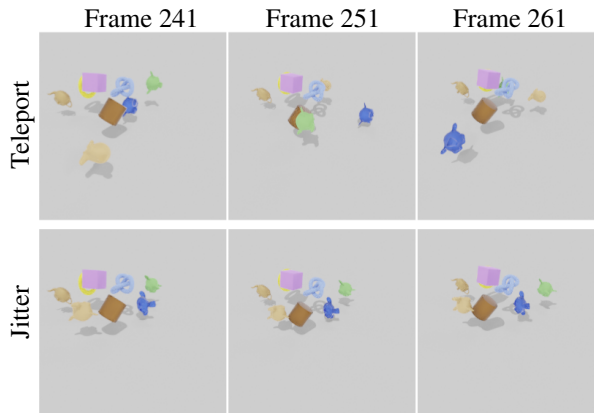


Figure 10. **Robust NeRF (training data)** – a dataset that violates the rigidity assumptions typically assumed by NeRF training workloads. Here, we qualitatively visualize the “teleport” and “jitter” versions of the training dataset.

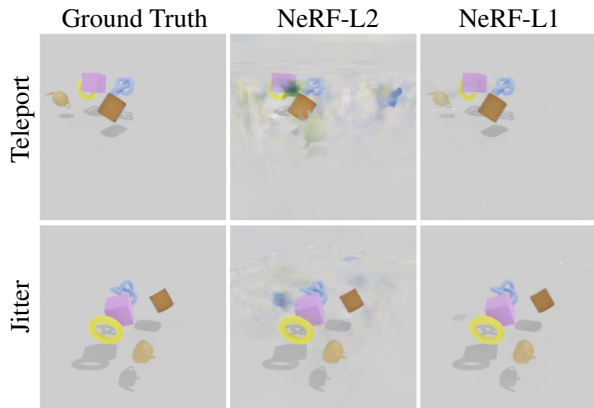


Figure 11. **Robust NeRF (training outcome)** – Visualizing the rendering of NerF-L2 vs Nerf-L1 for models trained on Teleport and Jitter training sets. During test the ground truth does not have dynamic objects. Typical NeRF-L2 models render a shadow in place of transient objects where as the NeRF-L1 model can successfully remove the floaters.

Classical methods involve active-contour [47, 69] or graph-cut [20, 104] techniques, but there also exist techniques with human-in-the-loop [72, 81, 100], and more recently deep learning variants [30, 73, 74, 105, 117]. With human feedback, interactive methods are typically robust, but also costly. Automatic segmentation, be it with traditional methods or deep networks, are less performant. Here we propose a

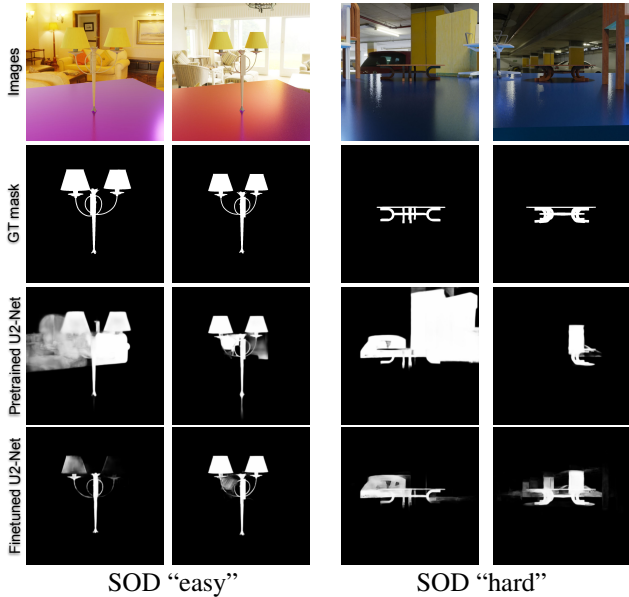


Figure 12. **Salient Object Detection** – Images, ground truth mask, as well as predictions from U^2 -Net (pretrained and fine-tuned) over an example scene in the easy and hard datasets.

new mode of operation in SOD, a significantly harder task (see Figure 12), yet with sufficient information for a human to solve the problem without ambiguity. We compare several single view state-of-the-art SOD algorithms on this dataset, and propose two datasets with increased complexity. Instead of one image, we assume access to *multiple* images (taken from different angles) of the same salient object. With multiple views of the same object, we theorize that automatic SOD would be more robust as the 3D structure implied from multiple images provides information that could help disambiguate boundaries of the target object. For the *easy* challenge, scenes only contain *one* salient object within the scene, while in the *hard* challenge we additionally insert clutter. All target objects are randomly selected from SHAPENETCORE V2 the background from POLYHAVEN HDRIs [115]. In the case of the *hard* challenge, clutter objects are also sampled randomly from SHAPENETCORE V2. We render 10 images for each scene, and export images and segmentation masks with Kubric. The training/test sets contains 1000/100 scenes respectively for both *easy* and *hard*.

To the best of our knowledge, multi-view SOD baselines do not exist. We therefore evaluate recent SOTA single-view SOD models as baselines. We first evaluate the pretrained models on the *easy* dataset, as summarized in Table 8. Some pretrained models (e.g. U^2 -Net) performs decently. Next, we fine-tune the best performing pretrained models (U^2 -Net and CPD) on the *easy* dataset. Despite U^2 -Net and CPD’s strong performance, however, multiview enabled SOD models should be stronger as the failure cases of single view

| | Lambertian | | Specular | |
|-----------------|--------------|--------------|--------------|--------------|
| | PSNR | SSIM | PSNR | SSIM |
| LFN [86] | 29.71 | 0.883 | 26.77 | 0.816 |
| PixelNeRF [114] | 32.11 | 0.922 | 29.96 | 0.885 |

Table 9. **Complex BRDFs** – Comparison of novel view synthesis results for specular vs. diffuse materials.

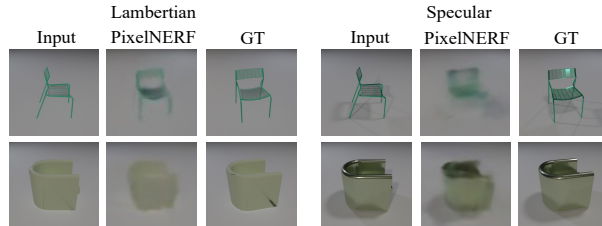


Figure 13. **Complex BRDFs** – Existing approaches struggle to model ShapeNet shapes rendered with specular materials.

SOD models (e.g. see Figure 12) indicate the lack of 3D understanding is often the culprit. Last but not least, we train U^2 -Net and CPD on the *easy* dataset from scratch for additional baseline results; see Table 8. We repeat the experiments on the *hard* dataset. In the presence of clutter, the task becomes significantly harder. Clutter is often mistaken to be the salient object especially when the objects are in close proximity. Again, the lack of 3D understanding is an important factor for the relative poor performance of the models. Models that work with multiple views, we hypothesize, will significantly improve upon the baselines.

4.8. Complex BRDFs

Consider the core vision problem of reconstructing a 3D scene from few observations [68, 86, 87, 114]. Current datasets [48, 114] mostly feature Lambertian scenes, i.e., scenes that consist of mostly diffuse surfaces, with few specular highlights. In this case, the only relevant scene parameters are the 3D geometry, as well as the *diffuse* surface color. When scene surfaces are highly reflective, the number of scene properties required for accurate novel view synthesis grows significantly. Instead of just 3D shape and appearance, the model needs to address 3D geometry, the BRDF of every surface point, as well as a full characterization of the light incident onto the scene. To this end, we render out a highly specular version of the ShapeNet dataset as a challenge for few-shot novel view synthesis algorithms. We follow Kato et al. [48] and render objects across 13 classes from the same 24 views. To each object, we randomly assign an RGB color. We place three light sources at randomized positions on the upper hemisphere. In this challenge, we fix the material properties of each object to the properties of the specular CLEVR [44], and ray-trace each scene with 12 ray bounces. We benchmark two recently proposed models on this dataset: Light Field Networks [86], which parameterizes

a scene via its 360-degree light field, and PixelNeRF [114], a conditional 3D-structured neural scene representation. In order for these models to successfully train and perform at test-time, they need to both model the view-dependent forward model correctly, and correctly infer the position of the light sources. We find that both models perform substantially worse in Table 9 and specular compared to Lambertian shapes. In Figure 13, we illustrate how existing approaches struggle to represent inherent specularities in shapes.

4.9. Single View Reconstruction

Reconstructing an explicit 3D representation of an object (e.g. polygonal mesh) exclusively from 2D image supervision is challenging due to the ill-posed nature of the problem. Given input 2D images and their associated 3D viewpoint parameters (i.e., comprising the azimuth, distance, and elevation of the camera looking at the object), current methods (e.g. SOFTRAS [58]) combine an encoder to first extract latent features from images followed by a decoder to extract 3D vertices and face connectivity from the encoded feature vectors. Next, a differentiable renderer can project the 3D faces according to the viewpoint and all while respecting view-dependent occlusion constraints. To train such a rasterization-based differentiable rendering model, a loss function can be formulated from the difference between this projected (i.e., rendered) output and an image of the silhouette of the object against ground-truth viewpoints. One common loss function is based on a soft IoU loss between the projected and ground-truth images. Notably, this entire optimization no longer relies on any direct 3D supervision on the explicit 3D object parameterization, only viewpoint labels are needed and these can be readily determined from sourcing camera responsible for producing the 2D supervision images.

We train a SOFTRAS [58] model on the *entire* SHAPENET-COREV2 dataset instead of the commonly-used subset of SHAPENET that only has 13-category, that’s typical for published work in this area [48, 58, 109]. The full SHAPENET-COREV2 consists of 55 categories with a total of approx. 51,300 object models. We leverage Kubric’s ability to automatically process these object models and project each into 24 random viewpoints, all while maintaining consistent meta information (camera pose and object category) that allows us to train SOFTRAS efficiently. We trained SoftRas on two experimental setups: “in-distribution”, for which we follow the training regimen of [58], train on 80% of each category, and test and report performance on the remaining 20% of each category, and “out-of-distribution” where we train on all categories except 4 classes that we leave out for testing. They are *train, tower, washer and vessel*. Our results for “in-distribution”, summarized in Figures 14 and 15, illustrate that we perform best on pillows and bowls (IoU 0.75

and 0.72), and worst on microphones and earphones (IoU 0.34). For “out-of-distribution” the results on the test classes are close to those reported in Figure 14, suggesting that SoftRas can generalize to new classes, but its limitations are on reconstructing images from classes with complex shapes like *headphones*. We observe that this processed dataset allows us to train a SOFTRAS capable of reconstructing a *wider range of objects* than in the original work of Liu et al. [58] but the performance for some classes are poor, which will hopefully inspire further research into more powerful and 2D-to-3D reconstruction methods.

4.10. Video Based Reconstruction

As discussed in Section 4.9, the ill-posed nature of single-shot 3D reconstruction makes it an extremely challenging task. To better supervise surface reconstruction, the extensive availability of video data provides an attractive alternative to images. Multi-frame consistency of video sequences imposes additional constraints. However, since most 3D scenes are not static and many interesting real-world objects are not rigid, it brings up a new challenge for video-based surface reconstruction methods to be robust to deformations.

LASR [111] presents a pipeline that jointly recovers object surface mesh, articulation, and camera parameters from a monocular video without using category-specific shape templates. The method first uses off-the-shelf networks to generate a mask (silhouette) of the main object and optical flow for each frame. Then, by leveraging SOFTRAS [58], LASR jointly optimizes the object’s rest shape, articulation, skinning weights, and camera parameters by minimizing the difference between the input and re-rendered color image, silhouette, and optical flow for each frame.

In this challenge, we first leverage Kubric to generate videos of both rigid (ShapeNet assets) and non-rigid⁴ objects to evaluate the general performance of LASR. As shown in Figure 16, LASR fits the mesh well with input views but fails to extrapolate to unseen views. As the optical flow loss has been demonstrated to be critical and the ground truth flow can never be obtained from real data, we also evaluate how much LASR relies on the accuracy of the flow estimation. We separately train LASR using either the estimated optical flow or the ground truth provided by Kubric and compare the results of reconstruction; see Table 10. As expected, training with the ground truth optical flow improves performance, although this improvement is marginal. Another fundamental limitation of LASR, as with many other mesh-based differentiable renderers, is that it assumes a *fixed* mesh topology and thus cannot handle topological changes. In Figure 16, we show an example where LASR fails to reconstruct a non zero genus shape (i.e. torus), highlighting the need for additional research towards more robust approaches.

⁴Human rigs imported from <https://quaternius.com>.

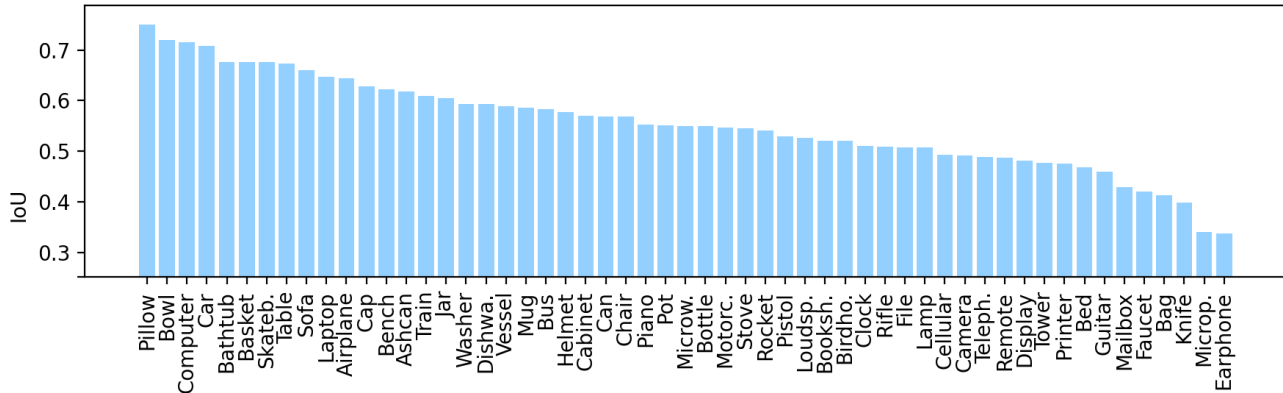


Figure 14. **Single View Reconstruction** – IoU results of training SoftRas on all ShapeNet categories. Pillows and bowls have the highest IoU and the model struggle’s most with microphones and earphones.

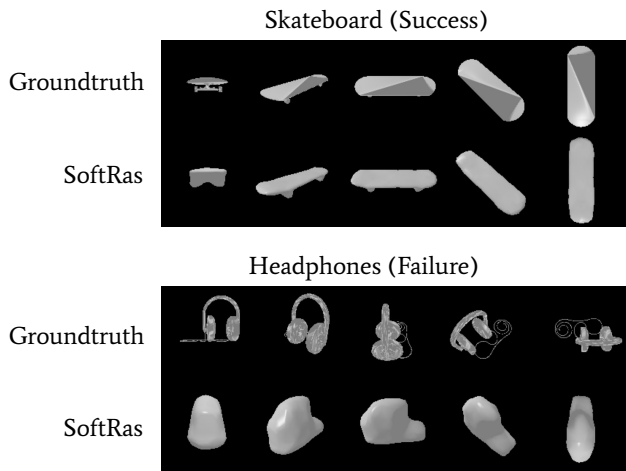


Figure 15. **Single View Reconstruction** – Qualitative results of SoftRas trained on the full ShapeNetCore V2 dataset of around 51,300 objects.

4.11. Point Tracking

The concept of optical flow can be easily extended to longer-term tracking, following the approach proposed in Tracking Any Point [3]. That is, given a video and a target point on a surface in the scene (specified in 2D), the goal is to output the 2D locations where that point appears in other video frames. This kind of motion inference has many applications, from 3D surface reconstruction, to inference of physical properties like center of gravity and elasticity, to memory of objects across long episodes for an interactive agent. Optical flow is insufficient in many of these domains because it cannot deal with occlusion, and small errors on frame pairs can lead to drift, resulting in large errors over time. It is straightforward to obtain long-term tracks from

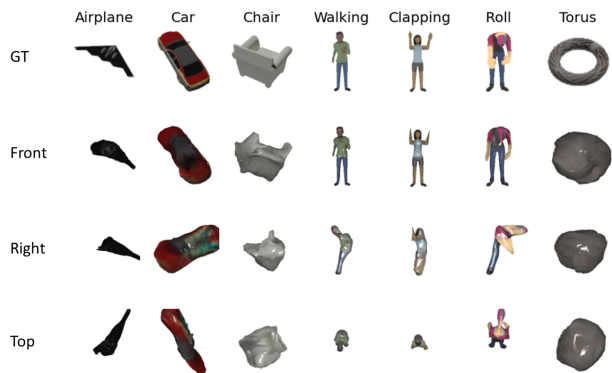


Figure 16. **Video Based Reconstruction** – Example results of 3D mesh reconstruction using LASR [111]. For each object class, we challenge LASR with a Kubric-generated 30-frame video consisting of the color image, object silhouette, and optical flow for each frame. We show the input (training) view of the object in the first row (GT). Others show the test views of the reconstructed object rendered from multiple viewing positions. Note that only the second row (Front) shares the same camera view as the input.

| Input | airplane | car | chair | walking | clapping | roll |
|----------------|-------------|-------------|-------------|-------------|-------------|-------------|
| True flow | 0.62 | 0.22 | 1.00 | 3.81 | 1.30 | 1.75 |
| Estimated flow | 1.52 | 0.26 | 1.08 | 3.19 | 1.34 | 1.85 |

Table 10. **Video Based Reconstruction** – Mesh reconstruction error measured by Chamfer Distance for each object with either the ground truth optical flow provided by Kubric or the estimated flow as training input.

Kubric by identifying a point on a 3D object, and then projecting that point throughout the scene. Large-scale training datasets for this problem are very difficult for humans to annotate, so synthetic data can serve a critical role in achieving good performance.

Given a video, the annotations consist of a set of trajectories, i.e. a set of 2D points $(x_{i,t}, y_{i,t}) \in \mathcal{R}^2$ where i

| method | AJ | $< \delta_{avg}^x$ | OA | Jac. δ^0 | Jac. δ^1 | Jac. δ^2 | Jac. δ^3 | Jac. δ^4 | $< \delta^0$ | $< \delta^1$ | $< \delta^2$ | $< \delta^3$ | $< \delta^4$ |
|-------------|------|--------------------|------|-----------------|-----------------|-----------------|-----------------|-----------------|--------------|--------------|--------------|--------------|--------------|
| Naïve | 28.6 | 44.7 | 82.1 | 9.7 | 16.2 | 25.8 | 38.5 | 52.9 | 18.2 | 28.6 | 42.6 | 59.0 | 74.8 |
| Contrastive | 49.5 | 68.7 | 80.5 | 17.2 | 35.5 | 53.9 | 67.1 | 73.6 | 30.8 | 55.1 | 75.0 | 88.0 | 94.2 |

Table 11. **Point Tracking** – Performance of our contrastive point tracking baseline. Jac. δ^x is the Jaccard metric measuring both occlusion estimation and point accuracy, with a threshold of δ^x ; AJ is the Average Jaccard across x between 0 and 4. $< \delta^x$ is the fraction of points not occluded in the ground truth for which the prediction is less than δ^x , and $< \delta_{avg}^x$ is the average across x between 0 and 4. Occlusion Accuracy is denoted with OA. We set $\delta = 2$.

| method | AJ | $< \delta_{avg}^x$ | OA | Jac. δ^0 | Jac. δ^1 | Jac. δ^2 | Jac. δ^3 | Jac. δ^4 | $< \delta^0$ | $< \delta^1$ | $< \delta^2$ | $< \delta^3$ | $< \delta^4$ |
|-------------|------|--------------------|------|-----------------|-----------------|-----------------|-----------------|-----------------|--------------|--------------|--------------|--------------|--------------|
| Naïve | 28.6 | 44.7 | 82.1 | 9.7 | 16.2 | 25.8 | 38.5 | 52.9 | 18.2 | 28.6 | 42.6 | 59.0 | 74.8 |
| Contrastive | 45.2 | 63.6 | 80.2 | 12.6 | 28.9 | 48.8 | 64.1 | 71.8 | 23.7 | 47.0 | 69.9 | 85.1 | 92.4 |

Table 12. **Point Tracking** – Performance for on vertically flipped videos from the evaluation dataset. We see a roughly 4% loss in performance on the average Jaccard score, suggesting that our method somewhat overfits to the scene layout. However, the performance is far from collapsing.

indexes the different tracked points, and t indexes time. The ground truth also includes $v_{i,t} \in \{0, 1\}$, which indicates whether a point i is visible in frame t is visible ($v_{i,t} = 1$) or not ($v_{i,t} = 0$). The tracking algorithm receives one visible point (x_i^*, y_i^*, t_i^*) for each trajectory, and must output an estimate $(\hat{x}_{i,t}, \hat{y}_{i,t})$ for the other frames, as well as a visibility prediction $\hat{v}_{i,t} \in \{0, 1\}$.

Metrics. We use three metrics proposed for Tracking Any Point [3]. The first ignores the output positions and evaluates occlusion estimation alone, via a simple classification accuracy which gives equal weight to each point on each frame. The second metric evaluates only tracking accuracy. Frames marked as occluded in the ground truth are ignored. For the rest, we report a PCK-style [2] accuracy across several different thresholds. That is, for a given threshold α , which is a distance in pixels, we consider a point correct if $\sqrt{(x_{i,t} - \hat{x}_{i,t})^2 + (\hat{y}_{i,t} - y_{i,t})^2} < \alpha$. Our final metric combines both classification accuracy and detection accuracy, and is inspired by the Jaccard-style metrics from the object tracking literature [60]. Let TP_α be the set of true positives: that is, all visible ground-truth points $(x_{i,t}, y_{i,t})$ for which $(\hat{x}_{i,t}, \hat{y}_{i,t})$ is predicted as unoccluded, and the spatial prediction is within a distance of α . Let FN_α be false negatives: visible ground truth points which are predicted to be occluded, or for which the predicted spatial position is farther than α from the ground truth. Let FP_α be false positives: points $(\hat{x}_{i,t}, \hat{y}_{i,t})$ which are predicted to be visible, where the ground truth is farther than distance α or where the ground truth is marked as occluded. The Jaccard metric is then $|TP_\alpha| / (|TP_\alpha| + |FN_\alpha| + |FP_\alpha|)$. In practice, we compute these metrics across 5 different thresholds of the form $\alpha = \delta^x$ pixels, for $x \in \{0, 1, 2, 3, 4\}$ and $\delta = 2$. We compute an average across thresholds to get an overall metric.

Baselines. We next define a baseline method that can be-

gin to solve the point tracking problem. One of the closest problems in the literature is segment tracking, using datasets like DAVIS [70]. Therefore, our baseline is inspired by VFS [108], a state-of-the-art method for DAVIS. VFS has two key components: first, a self-supervised training phase where the aim is to learn a good similarity metric between points across images, and second, a test-time tracking algorithm based on earlier work [101] which can associate points in unlabeled frames with the points in labeled frames. Our model, however, is modified to deal with points rather than segments, and to leverage the labeled training data we have available. For pre-training, we adopt a contrastive approach [39]. We use a standard ResNet-50 [38] as a backbone, up to the final convolution, and with stride = 1 for the final two blocks, which gives us a feature grid F_i (which is $L2$ -normalized over channel axis) for each frame, at stride 8. Given a query point, (x^*, y^*, t^*) (note: we drop the i index for clarity as we consider a single point), we first extract a feature f^* for that point, via bilinear interpolation at position $(x^*/8, y^*/8)$ from the feature grid for frame t^* . We then compute the following contrastive loss function:

$$\sum_{f_j \in F_i} \gamma_j \log \left(\frac{\exp(f_i^* \cdot f_j) / \tau}{\sum_k \exp(f_i^* \cdot f_k / \tau)} \right) \quad (1)$$

where j and k index over the spatio-temporal dimensions of F . The temperature hyperparameter τ is set to 0.1. γ_j is the source of supervision: its value is high if f_j is in correspondence with f^* , and it is 0 if they aren't. Note that if there is exactly one other point considered to be "in correspondence" with f^* , then the sum over k has a single term, and we are left with a standard contrastive loss. However, in our case, we have multiple potential correspondences, and this loss encourages all of them to have roughly equally high dot products.

We compute γ_j via bilinear interpolation. Say that the

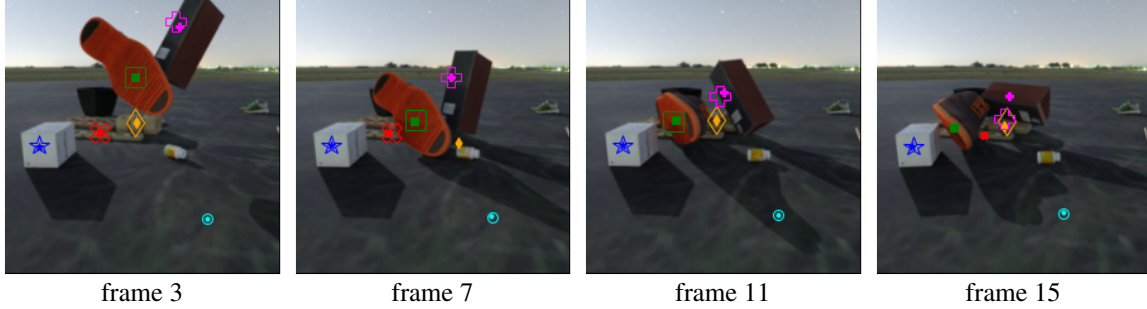


Figure 17. **Point Tracking** – Visualization of points tracked using our contrastive learning algorithm. We show each of 6 tracked points with a different symbol and color, where the smaller, filled symbol is the prediction, while the larger, unfilled symbol is the ground truth. If the ground truth is occluded or the point is predicted to be occluded, the corresponding symbol is not shown. We show only frames 3, 7, 11, and 15 out of a full 24-frame sequence for brevity. Note that the query frame is not necessarily at the beginning. The query was in frame 3 for the cyan circle, the green square, and the red X; frame 7 for the blue star and the magenta plus, and frame 11 for the orange diamond.

feature f_j is on frame t at position \hat{x}, \hat{y} within the convolutional feature grid, and the ground truth position is at $(x_t/8, y_t/8)$ (in the coordinate frame of the feature grid). If $(x_t/8, y_t/8)$ lies within the grid cell which has one of its corners at \tilde{x}_j, \tilde{y}_j , then we set $\gamma_j = (1 - |\tilde{x}_k - x_t/8|) * (1 - |\tilde{y}_k - y_t/8|)$. Otherwise, it is 0. γ_j is also set to 0 if the ground truth is marked as occluded for frame t .

At test time, given a query point (x^*, y^*, t^*) , we begin by computing a correspondence to every frame. For a single frame at time t , this is done via a dot product between f^* (again extracted via bilinear interpolation) and each feature in frame t , followed by a softmax S across space, which gives us a heatmap of likely locations, i.e., S_{xy} is the probability that x, y corresponds to (x^*, y^*, t^*) . We then compute \hat{S} by finding the argmax of S and zeroing out any grid cells further than 40 pixels away (5 grid units) from it, to suppress potential multimodal correspondences. Then we compute the weighted average of the potential locations $[\hat{x}, \hat{y}] = \sum_{x,y} [x, y] * \hat{S}_{xy} / \sum_{x,y} \hat{S}_{xy}$.

In order to classify whether the point is occluded, we use cycle consistency [99, 101]. That is, we extract a new feature \hat{f} from point $[\hat{x}, \hat{y}]$ in frame t , and reverse the process, computing a softmax over locations in frame t^* and converting it into a point correspondence. If the estimated point is further than 48 pixels of its starting location, we consider it occluded.

We evaluate this procedure on MOVi-E at a resolution of 256×256 . For each evaluation video, we sample 256 query points randomly across all frames. We attempt to sample an equal number of points from each object as well as the background, but cap the number of samples per object at a maximum of 0.2% of the visible pixels. We use standard data augmentations, including a random crop of the image as small as 30% of the image area and an aspect ratio between 2:1 and 1:2, and the same color augmentations and pixel noise that was used for our optical flow experiments.

Results are shown in Table 11. For comparison, we also include a naive baseline which assumes no motion and no occlusion, which is the best that can be done without reference to the pixels. We see that the contrastive approach is fairly good at coarse tracking, reducing the error rate on the largest threshold from 25.2% down to just 5.8%, a reduction of more than 6 times relative to the naive baseline. However, for more precise tracking, the reduction in error is not nearly as great. On the other hand, accuracy at detecting occlusions is quite poor for this method; for the threshold we used for cycle consistency (48), the accuracy is actually worse than chance. However, points for which the cycle consistency check failed are actually unlikely to be within any distance threshold; therefore, we find that removing these points from the output improves the average Jaccard metric.

Because the network is trained and evaluated on data from the same distribution, there is a possibility that the algorithm is memorizing some aspects of the training data, such as the common trajectories followed by objects. To evaluate out-of-distribution transfer, we also applied our algorithm to vertically-flipped videos, and show the results in Table 12. This harms performance by about 4%, suggesting that the network is memorizing trajectories to a small extent.

Finally, Figure 17 shows a qualitative example of our point tracking algorithm on a kubric validation video. We see that for easy points with relatively little motion, like the blue star or cyan circle, the algorithm is quite accurate, even when there is relatively little texture. Tracking can also be good for the points that have reasonably distinctive texture, like the green square. Occlusions are also sometimes detected correctly: for the red X, the algorithm correctly determines the occlusion on frame 11, although it prematurely finds the point again on frame 15. However, there are also obvious failures: for instance, the algorithm loses the magenta plus, likely because the object has rotated so much that the appearance has changed substantially. This suggests that

| | | KLEVR | ToyBox5 | ToyBox13 |
|----|--------------------|-------|---------|----------|
| 2D | DeepLab [15] | 97.1% | 81.6% | 63.1% |
| | NeSF [97] | 92.7% | 81.9% | 56.5% |
| 3D | SparseConvNet [35] | 99.7% | 93.4% | 83.2% |
| | NeSF [97] | 97.8% | 88.7% | 60.1% |

Table 13. **Scene Semantic Segmentation** – We compare mean intersection-over-union in 2D image segmentation (top) and 3D point cloud segmentation (bottom) on the three datasets.

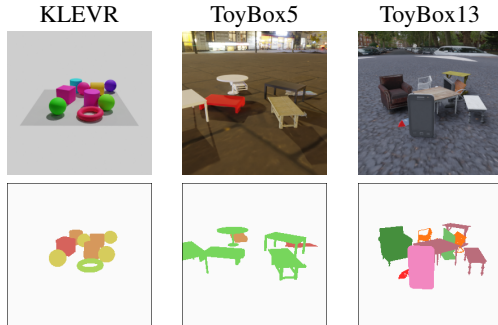


Figure 18. **Scene Semantic Segmentation** – Example RGB and segmentation renders from the datasets.

it may be useful to employ global reasoning about the orientation of objects rather than relying on appearance alone. We also see a very large error for the diamond on frame 7, when the point is occluded; the algorithm instead places the point between the occluder objects, possibly because the feature descriptors are relying too heavily on context. This result suggests that simultaneously capturing global object motion while remaining robust to occlusion will be a substantial challenge in this dataset moving forward.

4.12. Scene Semantic Segmentation

As another use case, we consider the task of comparing 2D and 3D semantic segmentation models. As these methods operate on fundamentally different substrates, it is challenging to quantify the effectiveness of one method versus another. To this end, we construct three synthetic datasets where 2D image and 3D point cloud are in direct correspondence: KLEVR, ToyBox5 and ToyBox13. Each of the ToyBox datasets each consists of 525 scenes. Each scene contains 4-12 upright ShapeNet objects on a flat surface with one of 382 randomly chosen HDRI backdrops. The datasets differ only in the set of ShapeNet objects employed. In ToyBox5, we use the top 5 most common object categories; in ToyBox13, the 13 most common object categories. For each scene, we select 300 camera poses and render 3 images per pose: an RGB map, a segmentation map, and a depth map. With knowledge of camera parameters, we are able to construct a camera ray $\mathbf{r}(t) = \mathbf{o} + t\mathbf{d}$ corresponding

| | PSNR | SSIM | LPIPS |
|-----------------|-------|-------|-------|
| LFN [86] | 14.77 | 0.328 | 0.582 |
| PixelNeRF [114] | 21.97 | 0.689 | 0.332 |
| SRT [82] | 23.41 | 0.697 | 0.369 |

Table 14. **Conditional Novel View Synthesis** – Quantitative evaluation for novel view synthesis.



Figure 19. **Conditional Novel View Synthesis** – The scenes are very difficult as they contain a large number of objects in random poses, contain realistic backgrounds, and are rendered with ray-tracing. LFN fails to capture these datasets in a global latent, severely under-fitting. PixelNeRF shows better quality renders, which however degrade for out-of-training distribution target views (e.g., bottom row).

to each pixel in the dataset. When combined with depth and segmentation maps, we obtain a labeled 3D point cloud where each 3D point corresponds to one camera pixel. We define a scene’s point cloud to be the union of all 3D points constructed from all camera poses. The KLEVR dataset is constructed identically to the ToyBox datasets except with a fixed, neutral-grey backdrop and 5 platonic object shapes.

Experiments. We demonstrate two representative baselines for 2D image and 3D point cloud segmentation: DeepLab [15] and SparseConvNet [35], respectively. In addition, we compare these methods with NeSF [97], a method for dense 2D and 3D scene segmentation from posed RGB images. We train all methods with semantic supervision derived from 9 cameras per scene from 500 scenes and hold out 4 cameras per scene from the remaining 25 scenes for evaluation. In 2D, we see that NeSF and DeepLab perform similarly, with DeepLab outperforming NeSF by 0.3% to 6.6% (Table 13). In qualitative results, we find that DeepLab’s predictions more tightly outline objects at the expense of multiview consistency. In 3D, we see that SparseConvNet achieves between 1.9% and 23.1% higher mean intersection-over-union than NeSF with larger margins as dataset complexity increases. We attribute this to the SparseConvNet’s access to ground truth 3D geometry and supervision in the form of a dense point cloud. This results in an exceedingly dense and accurate representation of 3D geometry. NeSF, on the other hand, must infer 3D geometry and semantics from posed 2D images alone. Further results and comparison to NeSF are presented in [97].

4.13. Conditional Novel View Synthesis

Neural scene representations such as [66] have led to state-of-the-art results in novel-view synthesis tasks on real-world datasets [63], however, a new model must be trained on each new scene, which does not allow the model to learn a *prior* over the dataset. Prior works commonly use the ShapeNet dataset [14] to evaluate how well a method can generalize to novel scenes [86, 114]. However, ShapeNet consists of *canonically* oriented objects with thousands of same-class examples for some categories (*e.g.*, airplanes) rendered with flat shading. We introduce a new large-scale dataset using Kubric to generate photo-realistic scenes with groups of ShapeNet objects. Each of the 1M scenes use one of 382 randomly chosen background maps. We render ten 128×128 random views for each scene and use five as *conditioning views*, and the other five as *target views*. The task is to reconstruct the target views *given* the conditioning views. We compare the following recent methods: PixelNeRF [114], which projects points into the conditioning views to interpolate encoded image features, LFN [86], which condenses the scene into a single latent code, and decodes it into an implicit scene representation using a hypernetwork that produces the weights of the scene-specific MLP, and SRT [82], which learns a scalable set-latent scene representation through a transformer encoder-decoder architecture. Fig. 19 compares these methods on our new challenge. While all methods above produce fairly high-quality results on ShapeNet (see [82]), they scale vastly differently to our photorealistic, complex dataset: while PixelNeRF has apparent difficulties with views that are far away from the conditioning views, LFN does not scale at all to this complexity, and SRT’s reconstructions suffer from blurriness. Further details on this challenge and the dataset release are presented in [82].

5. Conclusions

We introduce Kubric, a general Python framework complete with tools for generation at scale, integrating assets from multiple sources, rich annotations and a common export data format (SunDS) for porting data directly into training pipelines. Kubric enables the generation of high quality synthetic data, addressing many of the problems inherent in curating natural image data, and circumventing the expense of building task-specific, one-off pipelines. We demonstrate the effectiveness of our framework in 11 case studies with generated datasets of varying complexity for a range of different vision tasks. In each case, Kubric has substantially reduced the engineering effort to generate the required data and has facilitated reuse and collaboration. We hope that it will help the community by lowering the barriers to generating high-quality synthetic data, reduce fragmentation, and facilitate the sharing of pipelines and datasets.

Limitations and future work. While already tremendously useful, Kubric is still a work in progress and does not yet support many features of Blender and PyBullet. Notable examples include volumetric effects like fog or fire, soft-body and cloth simulations, and advanced camera effects such as depth of field and motion blur. We also plan to preprocess and unify assets from more sources, including the ABC dataset [51] or Amazon Berkeley Objects [17]. At present, Kubric requires substantial computational resources due to its reliance on a path-tracing renderer versus a rasterizing renderer. We hope to add support for a rasterizing backend, allowing users to trade-off speed and render quality.

We include a discussion on the potential societal impact and ethical implications surrounding the application of our system in Section 6 of the supplementary material.

6. Societal Impact and Ethical Considerations

The diversity of applications that can leverage our system merits a broad discussion on both its potential societal impact and the ethical considerations one should consider when applying it. As a general purpose tool rather than an application-targeted solution, Kubric bears the potential for diverse benefits as well as the risk of harm through negligence or even malicious misuse.

Societal Impact. Synthetic dataset construction presents system engineers with the opportunity to detect and correct potentially dangerous failure modes – particularly for those applications that involve human interaction, *e.g.*, self-driving cars and robotics – *prior to* their deployment in the wild and with real humans. This does not, however, eliminate the possibility of developing systems that could cause serious injury to humans; instead, it raises the importance of considering the possibility of such outcomes. We therefore urge Kubric users that work towards systems deployed outside the laboratory, to take *active* measures towards mitigating such risks and consider them at the forefront of the design process. Still, the potential value of leveraging synthetic dataset construction as a tool to help guard against harmful outcomes should be further explored.

Ethical Considerations. While Kubric’s dataset generation relies on human-driven design automation, it sidesteps the immediate need for human-derived data. This can help to avoid ethical problems and legal obstacles to research and can also be a powerful tool for studying and mitigating undesirable societal biases. Still, any human-in-the-loop semi-automated processes are susceptible to the biases of their designers. While a more explicitly-controlled dataset design methodology allows engineers to postpone complications surrounding the (important) privacy concerns due to the treatment of data captured from the real-world, one can reasonably argue that such a benefit is offset – at least in part – by biases introduced during the dataset synthesis

process. Indeed, any explicitly-constructed synthetic dataset will be vulnerable to inheriting the biases of the processes employed when constructing it – but we argue that it promotes the discussion and (hopefully) the mitigation of biases at *both* an earlier stage of the design process *and* with a greater degree of controllability. The potential downstream impacts of distributional differences between the synthetic and real-world data would then become an important additional concern, requiring explicit evaluation and potential mitigation/treatment to safeguard against real world bias.

We also note that, while Kubric, on the one hand, provides an effective way to create new datasets, helping to avoid becoming stuck on, and over-fitting to existing data, it may also, on the other hand, enable the proliferation of datasets tailored to highlight the advantages of one’s method of choice. While this is true with all dataset creation, it is hoped that through experimentation and replication, as with model architectures, the field will self-select datasets that are useful, providing fair, balanced assessment of different models on tasks of common interest.

Environmental considerations. Controllable synthetic dataset construction helps to promoting a control-based scientific methodology: e.g., where confounding factors can be explicitly isolated and tested against, and by allowing smaller problems to be constructed (i.e., where only those behaviors one seeks to validate are tested against) before scaling to larger, more general settings. This strategy can help to reduce the need for repeatedly training large-scale models on huge datasets, and thus lower the overall environmental impact of the research project. However, the ability of to generate large and controllable synthetic datasets does not come without its costs; for example, our optical flow dataset required roughly 3 CPU-years of compute-time. Hence we urge researchers to be mindful of the costs of both training and generating datasets, and to avoid generating unnecessarily large datasets. As such, the design of surrogate synthesis models capable of augmenting synthetic datasets in a more energy-efficient fashion, e.g., with latent-space dynamical models, is an important line of future research.

Synopsis. Synthetic data offers the opportunity for researchers and engineers to consider and face the impact of bias on their systems, to design around detecting dangerous failure modes, and all in a privacy-preserving setting. This certainly does not preclude the presence of such issues in any resulting final system, as the manner and degree in which these opportunities are leveraged should mandate an additional level of responsibility during the design and meta-evaluation of the synthetic datasets.

References

[1] Radhakrishna Achanta, Sheila Hemami, Francisco Estrada, and Sabine Susstrunk. Frequency-tuned salient region de-

tection. In *2009 IEEE conference on computer vision and pattern recognition*, pages 1597–1604. IEEE, 2009. 9

[2] Mykhaylo Andriluka, Leonid Pishchulin, Peter Gehler, and Bernt Schiele. 2d human pose estimation: New benchmark and state of the art analysis. In *Proceedings of the IEEE Conference on computer Vision and Pattern Recognition*, pages 3686–3693, 2014. 13

[3] Anonymous Authors. TAP-Net: Tracking any point in a video. In *Submission*, 2022. 12, 13

[4] Yuki M. Asano, Christian Rupprecht, Andrew Zisserman, and Andrea Vedaldi. Pass: An imagenet replacement for self-supervised pretraining without humans. *NeurIPS Track on Datasets and Benchmarks*, 2021. 2

[5] Aharon Azulay and Yair Weiss. Why do deep convolutional networks generalize so poorly to small image transformations?, 2019. 2

[6] S Baker, D Scharstein, JP Lewis, S Roth, MJ Black, and R Szeliski. A database and evaluation methodology for optical flow. *International Journal of Computer Vision*, 92:1–31, 2011. 2

[7] J. L. Barron, D. J. Fleet, and S. S. Beauchemin. Performance of optical flow techniques. *International Journal of Computer Vision*, 12:43–77, 1994. 2, 7

[8] Abeba Birhane and Vinay Uday Prabhu. Large image datasets: A pyrrhic win for computer vision? In *IEEE Winter Conference on Applications of Computer Vision, WACV 2021, Waikoloa, HI, USA, January 3-8, 2021*, pages 1536–1546. IEEE, 2021. 8

[9] Blender Online Community. *Blender - a 3D modelling and rendering package*. Blender Foundation, Blender Institute, Amsterdam, 2021. 2

[10] Ali Borji, Ming-Ming Cheng, Huaizu Jiang, and Jia Li. Salient object detection: A benchmark. *IEEE transactions on image processing*, 24(12):5706–5722, 2015. 9

[11] Steve Borkman, Adam Crespi, Saurav Dhakad, Sujoy Ganguly, Jonathan Hogins, You-Cyuan Jhang, Mohsen Kamalzadeh, Bowen Li, Steven Leal, Pete Parisi, Cesar Romero, Wesley Smith, Alex Thaman, Samuel Warren, and Nupur Yadav. Unity perception: Generate synthetic data for computer vision, 2021. 2

[12] Christopher P Burgess, Loic Matthey, Nicholas Watters, Rishabh Kabra, Irina Higgins, Matt Botvinick, and Alexander Lerchner. MONet: Unsupervised scene decomposition and representation. *arXiv preprint arXiv:1901.11390*, 2019. 7

[13] D. J. Butler, J. Wulff, G. B. Stanley, and M. J. Black. A naturalistic open source movie for optical flow evaluation. In A. Fitzgibbon et al. (Eds.), editor, *European Conf. on Computer Vision (ECCV)*, Part IV, LNCS 7577, pages 611–625. Springer-Verlag, Oct. 2012. 2

[14] Angel X Chang, Thomas Funkhouser, Leonidas Guibas, Pat Hanrahan, Qixing Huang, Zimo Li, Silvio Savarese, Manolis Savva, Shuran Song, Hao Su, Jianxiong Xiao, Li Yi, and Fisher Yu. ShapeNet: An Information-Rich 3D model repository. Dec. 2015. 5, 16

[15] Liang-Chieh Chen, George Papandreou, Iasonas Kokkinos, Kevin Murphy, and Alan L Yuille. Deeplab: Semantic

- image segmentation with deep convolutional nets, atrous convolution, and fully connected crfs. *IEEE transactions on pattern analysis and machine intelligence*, 40(4):834–848, 2017. 15
- [16] Yuhua Chen, Wen Li, Xiaoran Chen, and Luc Van Gool. Learning semantic segmentation from synthetic data: A geometrically guided input-output adaptation approach. In *Proceedings of the IEEE/CVF Conference on Computer Vision and Pattern Recognition (CVPR)*, June 2019. 2
- [17] Jasmine Collins, Shubham Goel, Achleshwar Luthra, Leon Xu, Kenan Deng, Xi Zhang, Tomas F Yago Vicente, Himanshu Arora, Thomas Dideriksen, Matthieu Guillaumin, and Jitendra Malik. ABO: Dataset and benchmarks for Real-World 3D object understanding. Oct. 2021. 16
- [18] E Coumans and Y Bai. Pybullet, a python module for physics simulation for games, robotics and machine learning. 2016. 4
- [19] Erwin Coumans and Yunfei Bai. Pybullet, a python module for physics simulation for games, robotics and machine learning. 2016. 5
- [20] Ingemar J Cox, Satish B Rao, and Yu Zhong. "ratio regions": a technique for image segmentation. In *Proceedings of 13th International Conference on Pattern Recognition*, 1996. 9
- [21] Angela Dai, Angel X Chang, Manolis Savva, Maciej Halber, Thomas Funkhouser, and Matthias Nießner. Scannet: Richly-annotated 3d reconstructions of indoor scenes. In *Proceedings of the IEEE conference on computer vision and pattern recognition*, pages 5828–5839, 2017. 2
- [22] Dawson-Haggerty et al. trimesh. 5
- [23] M Denninger, M Sundermeyer, and others. Blenderproc. *arXiv:1911.01911*, 2019. 2, 3
- [24] Carl Doersch and Andrew Zisserman. Sim2real transfer learning for 3d pose estimation: motion to the rescue. *NeurIPS*, pages 12949–12961, 2019. 2
- [25] Alexey Dosovitskiy, Lucas Beyer, Alexander Kolesnikov, Dirk Weissenborn, Xiaohua Zhai, Thomas Unterthiner, Mostafa Dehghani, Matthias Minderer, Georg Heigold, Sylvain Gelly, Jakob Uszkoreit, and Neil Houlsby. An image is worth 16x16 words: Transformers for image recognition at scale. In *9th International Conference on Learning Representations, ICLR 2021, Virtual Event, Austria, May 3-7, 2021*. OpenReview.net, 2021. 8
- [26] Alexey Dosovitskiy, Philipp Fischer, Eddy Ilg, Philip Häusser, Caner Hazirbas, Vladimir Golkov, Patrick van der Smagt, Daniel Cremers, and Thomas Brox. FlowNet: Learning optical flow with convolutional networks. In *2015 IEEE International Conference on Computer Vision (ICCV)*, pages 2758–2766, 2015. 2, 7
- [27] A Eftekhari, A Sax, and others. Omnidata: A scalable pipeline for making multi-task mid-level vision datasets from 3d scans. *arXiv:2110.04994*, 2021. 2
- [28] Martin Engelcke, Adam R Kosiorek, Oiwi Parker Jones, and Ingmar Posner. GENESIS: Generative scene inference and sampling with object-centric latent representations. In *International Conference on Learning Representations*, 2020. 7
- [29] Deng-Ping Fan, Ming-Ming Cheng, Yun Liu, Tao Li, and Ali Borji. Structure-measure: A new way to evaluate foreground maps. In *Proceedings of the IEEE international conference on computer vision*, pages 4548–4557, 2017. 9
- [30] Deng-Ping Fan, Ge-Peng Ji, Guolei Sun, Ming-Ming Cheng, Jianbing Shen, and Ling Shao. Camouflaged object detection. In *Proceedings of the IEEE/CVF conference on computer vision and pattern recognition*, pages 2777–2787, 2020. 9
- [31] Blender Foundation. Blender 2.93.6 release candidate python api documentation, 2021. 3
- [32] Maayan Frid-Adar, Eyal Klang, Michal Amitai, Jacob Goldberger, and Hayit Greenspan. Synthetic data augmentation using gan for improved liver lesion classification. In *2018 IEEE 15th international symposium on biomedical imaging (ISBI 2018)*, pages 289–293. IEEE, 2018. 2
- [33] A Gaidon, Q Wang, Y Cabon, and E Vig. Virtual worlds as proxy for multi-object tracking analysis. *CVPR*, 2016. 2
- [34] C Gan, J Schwartz, and others. ThreeDWorld: A platform for interactive Multi-Modal physical simulation. *arXiv:2007.04954*, 2020. 2, 3
- [35] Benjamin Graham and Laurens van der Maaten. Sub-manifold sparse convolutional networks. *arXiv preprint arXiv:1706.01307*, 2017. 15
- [36] Klaus Greff, Raphaël Lopez Kaufman, Rishabh Kabra, Nick Watters, Christopher Burgess, Daniel Zoran, Loic Matthey, Matthew Botvinick, and Alexander Lerchner. Multi-object representation learning with iterative variational inference. In *International Conference on Machine Learning*, pages 2424–2433, 2019. 6, 7
- [37] Ankush Gupta, Andrea Vedaldi, and Andrew Zisserman. Synthetic data for text localisation in natural images. In *Proceedings of the IEEE Conference on Computer Vision and Pattern Recognition (CVPR)*, June 2016. 2
- [38] Kaiming He, Xiangyu Zhang, Shaoqing Ren, and Jian Sun. Deep residual learning for image recognition. In *Proceedings of the IEEE conference on computer vision and pattern recognition*, pages 770–778, 2016. 13
- [39] Olivier J Hénaff, Aravind Srinivas, Jeffrey De Fauw, Ali Razavi, Carl Doersch, SM Eslami, and Aaron van den Oord. Data-efficient image recognition with contrastive predictive coding. In *International Conference on Machine Learning*, pages 4182–4192. PMLR, 2020. 13
- [40] Stefan Hinterstoisser, Olivier Pauly, Hauke Heibel, Marek Martina, and Martin Bokeloh. An annotation saved is an annotation earned: Using fully synthetic training for object detection. In *Proceedings of the IEEE/CVF International Conference on Computer Vision (ICCV) Workshops*, Oct 2019. 2
- [41] Jingwei Huang, Yichao Zhou, and Leonidas Guibas. Manifoldplus: A robust and scalable watertight manifold surface generation method for triangle soups. *arXiv preprint arXiv:2005.11621*, 2020. 5
- [42] Lawrence Hubert and Phipps Arabie. Comparing partitions. *Journal of Classification*, 2(1):193–218, 1985. 6
- [43] S James, P Wohlhart, M Kalakrishnan, and others. Sim-to-real via sim-to-sim: Data-efficient robotic grasping via randomized-to-canonical adaptation networks. *Proceedings of the*, 2019. 4

- [44] Justin Johnson, Bharath Hariharan, Laurens van der Maaten, Li Fei-Fei, C Lawrence Zitnick, and Ross Girshick. CLEVR: A diagnostic dataset for compositional language and elementary visual reasoning. In *Proceedings of the IEEE Conference on Computer Vision and Pattern Recognition*, 2017. 2, 6, 10
- [45] Rishabh Kabra, Daniel Zoran, Loic Matthey Goker Erdogan, Antonia Creswell, Matthew Botvinick, Alexander Lerchner, and Christopher P. Burgess. SIMONE: View-invariant, temporally-abstracted object representations via unsupervised video decomposition. *arXiv preprint arXiv:2106.03849*, 2021. 6, 7
- [46] Dmitry Kalashnikov, Alex Irpan, Peter Pastor, Julian Ibarz, Alexander Herzog, Eric Jang, Deirdre Quillen, Ethan Holly, Mrinal Kalakrishnan, Vincent Vanhoucke, and Sergey Levine. QT-Opt: Scalable deep reinforcement learning for Vision-Based robotic manipulation. June 2018. 4
- [47] Michael Kass, Andrew Witkin, and Demetri Terzopoulos. Snakes: Active contour models. *International journal of computer vision*, 1988. 9
- [48] Hiroharu Kato, Yoshitaka Ushiku, and Tatsuya Harada. Neural 3d mesh renderer. In *Proc. CVPR*, pages 3907–3916, 2018. 10, 11
- [49] Kangyeol Kim, Sunghyun Park, Jaeseong Lee, Sunghyo Chung, Junsoo Lee, and Jaegul Choo. Animeceleb: Large-scale animation celebfaces dataset via controllable 3d synthetic models, 2021. 2
- [50] Thomas Kipf, Gamaleldin F. Elsayed, Aravindh Mahendran, Austin Stone, Sara Sabour, Georg Heigold, Rico Jonschkowski, Alexey Dosovitskiy, and Klaus Greff. Conditional Object-Centric Learning from Video. *arXiv preprint arXiv:2111.12594*, 2021. 6, 7
- [51] S Koch, A Matveev, Z Jiang, and others. ABC: A big cad model dataset for geometric deep learning. *Proceedings of the*, 2019. 16
- [52] Alexander Kolesnikov, Lucas Beyer, Xiaohua Zhai, Joan Puigcerver, Jessica Yung, Sylvain Gelly, and Neil Houlsby. Big transfer (bit): General visual representation learning. In Andrea Vedaldi, Horst Bischof, Thomas Brox, and Jan-Michael Frahm, editors, *Computer Vision - ECCV 2020 - 16th European Conference, Glasgow, UK, August 23-28, 2020, Proceedings, Part V*, volume 12350 of *Lecture Notes in Computer Science*, pages 491–507. Springer, 2020. 8, 9
- [53] Eric Kolve, Roozbeh Mottaghi, Winson Han, Eli VanderBilt, Luca Weihs, Alvaro Herrasti, Daniel Gordon, Yuke Zhu, Abhinav Gupta, and Ali Farhadi. Ai2-thor: An interactive 3d environment for visual ai, 2019. 3
- [54] Simon Kornblith, Jonathon Shlens, and Quoc V. Le. Do better imagenet models transfer better? In *IEEE Conference on Computer Vision and Pattern Recognition, CVPR 2019, Long Beach, CA, USA, June 16-20, 2019*, pages 2661–2671. Computer Vision Foundation / IEEE, 2019. 8
- [55] Alex Krizhevsky, Ilya Sutskever, and Geoffrey E. Hinton. Imagenet classification with deep convolutional neural networks. In Peter L. Bartlett, Fernando C. N. Pereira, Christopher J. C. Burges, Léon Bottou, and Kilian Q. Weinberger, editors, *Advances in Neural Information Processing Systems 25: 26th Annual Conference on Neural Information Processing Systems 2012. Proceedings of a meeting held December 3-6, 2012, Lake Tahoe, Nevada, United States*, pages 1106–1114, 2012. 8
- [56] Zhengqin Li, Ting-Wei Yu, Shen Sang, Sarah Wang, Sai Bi, Zexiang Xu, Hong-Xing Yu, Kalyan Sunkavalli, Milos Hasan, Ravi Ramamoorthi, and Manmohan Chandraker. Openrooms: An end-to-end open framework for photorealistic indoor scene datasets. *CoRR*, abs/2007.12868, 2020. 2
- [57] Tsung-Yi Lin, Michael Maire, Serge Belongie, James Hays, Pietro Perona, Deva Ramanan, Piotr Dollár, and C Lawrence Zitnick. Microsoft coco: Common objects in context. In *European conference on computer vision*, pages 740–755. Springer, 2014. 8
- [58] Shichen Liu, Tianye Li, Weikai Chen, and Hao Li. Soft rasterizer: A differentiable renderer for image-based 3d reasoning. In *Proceedings of the IEEE/CVF International Conference on Computer Vision*, pages 7708–7717, 2019. 11
- [59] Francesco Locatello, Dirk Weissenborn, Thomas Unterthiner, Aravindh Mahendran, Georg Heigold, Jakob Uszkoreit, Alexey Dosovitskiy, and Thomas Kipf. Object-centric learning with slot attention. In *Advances in Neural Information Processing Systems*, 2020. 7
- [60] Jonathon Luiten, Aljosa Osep, Patrick Dendorfer, Philip Torr, Andreas Geiger, Laura Leal-Taixé, and Bastian Leibe. Hota: A higher order metric for evaluating multi-object tracking. *International journal of computer vision*, 129(2):548–578, 2021. 13
- [61] Miles Macklin, Matthias Müller, Nuttapon Chentanez, and Tae-Yong Kim. Unified particle physics for real-time applications. *ACM transactions on graphics*, 33(4):1–12, July 2014. 3
- [62] Khaled Mamou, E Lengyel, and AK Peters. Volumetric hierarchical approximate convex decomposition. In *Game Engine Gems 3*, pages 141–158. AK Peters, 2016. 5
- [63] Ricardo Martin-Brualla, Noha Radwan, Mehdi S. M. Sajjadi, Jonathan T. Barron, Alexey Dosovitskiy, and Daniel Duckworth. NeRF in the Wild: Neural Radiance Fields for Unconstrained Photo Collections. In *CVPR*, 2021. 16
- [64] N Mayer, E Ilg, P Hausser, P Fischer, and others. A large dataset to train convolutional networks for disparity, optical flow, and scene flow estimation. In *CVPR*, 2016. 2
- [65] J McCormac, A Handa, and others. Scenet RGB-D: Can 5m synthetic images beat generic imagenet pre-training on indoor segmentation? In *CVPR*, 2017. 2
- [66] Ben Mildenhall, Pratul P. Srinivasan, Matthew Tancik, Ravi Ramamoorthi, and Ren Ng. Nerf: Representing scenes as neural radiance fields for view synthesis. In *ECCV*, 2020. 2, 9, 16
- [67] Pushmeet Kohli Nathan Silberman, Derek Hoiem and Rob Fergus. Indoor segmentation and support inference from rgb-d images. In *ECCV*, 2012. 2
- [68] Michael Niemeyer, Lars Mescheder, Michael Oechsle, and Andreas Geiger. Differentiable volumetric rendering: Learning implicit 3d representations without 3d supervision. In *Proc. CVPR*, 2020. 10

- [69] Stanley Osher and James A Sethian. Fronts propagating with curvature-dependent speed: Algorithms based on hamilton-jacobi formulations. *Journal of computational physics*, 1988. 9
- [70] Jordi Pont-Tuset, Federico Perazzi, Sergi Caelles, Pablo Arbeláez, Alex Sorkine-Hornung, and Luc Van Gool. The 2017 davis challenge on video object segmentation. *arXiv preprint arXiv:1704.00675*, 2017. 13
- [71] Senthil Purushwalkam and Abhinav Gupta. Demystifying contrastive self-supervised learning: Invariances, augmentations and dataset biases, 2020. 2
- [72] Xuebin Qin, Shida He, Zichen Zhang, Masood Dehghan, and Martin Jagersand. Bylabel: A boundary based semi-automatic image annotation tool. In *2018 IEEE Winter Conference on Applications of Computer Vision (WACV)*, 2018. 9
- [73] Xuebin Qin, Zichen Zhang, Chenyang Huang, Masood Dehghan, Osmar R Zaiane, and Martin Jagersand. U2-net: Going deeper with nested u-structure for salient object detection. *Pattern Recognition*, 106:107404, 2020. 9
- [74] Xuebin Qin, Zichen Zhang, Chenyang Huang, Chao Gao, Masood Dehghan, and Martin Jagersand. Basnet: Boundary-aware salient object detection. In *Proceedings of the IEEE/CVF Conference on Computer Vision and Pattern Recognition*, pages 7479–7489, 2019. 9
- [75] W Qiu and A Yuille. *UnrealCV: Connecting computer vision to unreal engine*. In *ECCV Workshops*. Springer, 2016. 2
- [76] Ali Sharif Razavian, Hossein Azizpour, Josephine Sullivan, and Stefan Carlsson. CNN features off-the-shelf: An astounding baseline for recognition. In *IEEE Conference on Computer Vision and Pattern Recognition, CVPR Workshops 2014, Columbus, OH, USA, June 23-28, 2014*, pages 512–519. IEEE Computer Society, 2014. 8
- [77] Google Research. Scanned objects dataset of common household objects, 2021. 5
- [78] S R Richter, V Vineet, S Roth, and V Koltun. Playing for data: Ground truth from computer games. In *ECCV*, 2016. 2
- [79] Fabrice Robinet, Rémi Arnaud, Tony Parisi, and Patrick Cozzi. gltf: Designing an open-standard runtime asset format. *GPU Pro*, 5:375–392, 2014. 5
- [80] G Ros, L Sellart, J Materzynska, and others. The synthia dataset: A large collection of synthetic images for semantic segmentation of urban scenes. In *CVPR*, 2016. 2
- [81] Bryan C Russell, Antonio Torralba, Kevin P Murphy, and William T Freeman. Labelme: a database and web-based tool for image annotation. *International journal of computer vision*, 2008. 9
- [82] Mehdi S. M. Sajjadi, Henning Meyer, Etienne Pot, Urs Bergmann, Klaus Greff, Noha Radwan, Suhani Vora, Mario Lucic, Daniel Duckworth, Alexey Dosovitskiy, Jakob Uszkoreit, Thomas Funkhouser, and Andrea Tagliasacchi. Scene Representation Transformer: Geometry-Free Novel View Synthesis Through Set-Latent Scene Representations. *CVPR*, 2022. 15, 16
- [83] Manolis Savva, Abhishek Kadian, Oleksandr Maksymets, Yili Zhao, Erik Wijmans, Bhavana Jain, Julian Straub, Jia Liu, Vladlen Koltun, Jitendra Malik, Devi Parikh, and Dhruv Batra. Habitat: A platform for embodied AI research. *CoRR*, abs/1904.01201, 2019. 3
- [84] Max Schwarz and Sven Behnke. Stilleben: Realistic scene synthesis for deep learning in robotics. *CoRR*, abs/2005.05659, 2020. 3
- [85] Jamie Shotton, Andrew Fitzgibbon, Mat Cook, Toby Sharp, Mark Finocchio, Richard Moore, Alex Kipman, and Andrew Blake. Real-time human pose recognition in parts from single depth images. In *CVPR 2011*, pages 1297–1304, 2011. 2
- [86] Vincent Sitzmann, Semon Rezkikov, William T. Freeman, Joshua B. Tenenbaum, and Fredo Durand. Light field networks: Neural scene representations with single-evaluation rendering. In *Proc. NeurIPS*, 2021. 10, 15, 16
- [87] Vincent Sitzmann, Michael Zollhöfer, and Gordon Wetzstein. Scene representation networks: Continuous 3d-structure-aware neural scene representations. In *Proc. NeurIPS*, 2019. 10
- [88] Deqing Sun, Charles Herrmann, Varun Jampani, Michael Krainin, Forrester Cole, Austin Stone, Rico Jonschkowski, Ramin Zabih, William T. Freeman, and Ce Liu. TF-RAFT: A tensorflow implementation of raft. In *ECCV Robust Vision Challenge Workshop*, 2020. 7
- [89] Deqing Sun, Daniel Vlasic, Charles Herrmann, Varun Jampani, Michael Krainin, Huiwen Chang, Ramin Zabih, William T Freeman, and Ce Liu. Autoflow: Learning a bet @articleMayer2016-xo, title = "A large dataset to train convolutional networks for disparity, optical flow, and scene flow estimation", author = "Mayer, N and Ilg, E and Hausser, P and Fischer, P and others", journal = "Proceedings of the", publisher = "openaccess.thecvf.com", year = 2016 ter training set for optical flow. In *CVPR*, 2021. 2, 7
- [90] Deqing Sun, Xiaodong Yang, Ming-Yu Liu, and Jan Kautz. PWC-Net: CNNs for optical flow using pyramid, warping, and cost volume. In *CVPR*, June 2018. 7
- [91] A Szot, A Clegg, and others. Habitat 2.0: Training home assistants to rearrange their habitat. *NeurIPS*, 2021. 2
- [92] Zachary Teed and Jia Deng. RAFT: Recurrent all-pairs field transforms for optical flow. In *ECCV*, 2020. 7
- [93] Thang To, Jonathan Tremblay, Duncan McKay, Yukie Yamaguchi, Kirby Leung, Adrian Balanon, Jia Cheng, William Hodge, and Stan Birchfield. NDDS: NVIDIA deep learning dataset synthesizer, 2018. https://github.com/NVIDIA/Dataset_Synthesizer. 3
- [94] Tatiana Tommasi, Novi Patricia, Barbara Caputo, and Tinne Tuytelaars. A deeper look at dataset bias, 2015. 2
- [95] Antonio Torralba and Alexei A Efros. Unbiased look at dataset bias. In *CVPR 2011*, pages 1521–1528. IEEE, 2011. 2
- [96] James Traer and Maddie Cusimano. A perceptually inspired generative model of rigid-body contact sounds. https://www.dafx.de/paper-archive/2019/DAFx2019_paper_57.pdf. Accessed: 2021-11-17. 3
- [97] Suhani Vora, Noha Radwan, Klaus Greff, Henning Meyer, Kyle Genova, Mehdi S. M. Sajjadi, Etienne Pot, Andrea Tagliasacchi, and Daniel Duckworth. Nesf: Neural semantic

- fields for generalizable semantic segmentation of 3d scenes. *arXiv preprint arXiv:2111.13260*, 2021. 15
- [98] Ronny Votel, Yu-Hui Chen, and Na Li. Next-generation pose detection with movenet and tensorflow.js, 2021. 8
- [99] Chaoyang Wang, Simon Lucey, Federico Perazzi, and Oliver Wang. Web stereo video supervision for depth prediction from dynamic scenes. In *2019 International Conference on 3D Vision (3DV)*, pages 348–357. IEEE, 2019. 14
- [100] Tinghuai Wang, Bo Han, and John Collomosse. Touchcut: Fast image and video segmentation using single-touch interaction. *Computer Vision and Image Understanding*, 2014. 9
- [101] Xiaolong Wang, Allan Jabri, and Alexei A Efros. Learning correspondence from the cycle-consistency of time. In *Proceedings of the IEEE/CVF Conference on Computer Vision and Pattern Recognition*, pages 2566–2576, 2019. 13, 14
- [102] Daniel Ward, Peyman Moghadam, and Nicolas Hudson. Deep leaf segmentation using synthetic data. *arXiv preprint arXiv:1807.10931*, 2018. 2
- [103] Erroll Wood, Tadas Baltrušaitis, Charlie Hewitt, Sebastian Dziadzio, Matthew Johnson, Virginia Estellers, Thomas J. Cashman, and Jamie Shotton. Fake it till you make it: Face analysis in the wild using synthetic data alone, 2021. 2, 8
- [104] Zhenyu Wu and Richard Leahy. An optimal graph theoretic approach to data clustering: Theory and its application to image segmentation. *IEEE transactions on pattern analysis and machine intelligence*, 1993. 9
- [105] Zhe Wu, Li Su, and Qingming Huang. Cascaded partial decoder for fast and accurate salient object detection. In *Proceedings of the IEEE/CVF Conference on Computer Vision and Pattern Recognition*, pages 3907–3916, 2019. 9
- [106] Fei Xia, William B Shen, Chengshu Li, Priya Kasimbeg, Michael Edmond Tchampi, Alexander Toshev, Roberto Martín-Martín, and Silvio Savarese. Interactive gibbon benchmark: A benchmark for interactive navigation in cluttered environments. *IEEE Robotics and Automation Letters*, 5(2):713–720, 2020. 2, 3
- [107] F Xia, A R Zamir, Z He, A Sax, J Malik, and others. Gibson env: Real-world perception for embodied agents. *Proceedings of the*, 2018. 4
- [108] Jiarui Xu and Xiaolong Wang. Rethinking self-supervised correspondence learning: A video frame-level similarity perspective. In *IEEE International Conference on Computer Vision (ICCV)*, 2021. 13
- [109] Xinchun Yan, Jimei Yang, Ersin Yumer, Yijie Guo, and Honglak Lee. Perspective transformer nets: Learning single-view 3d object reconstruction without 3d supervision. *arXiv preprint arXiv:1612.00814*, 2016. 11
- [110] Gengshan Yang and Deva Ramanan. Volumetric correspondence networks for optical flow. In *Advances in neural information processing systems*, pages 794–805, 2019. 7
- [111] Gengshan Yang, Deqing Sun, Varun Jampani, Daniel Vlasic, Forrester Cole, Huiwen Chang, Deva Ramanan, William T Freeman, and Ce Liu. Lasr: Learning articulated shape reconstruction from a monocular video. In *CVPR*, 2021. 11, 12
- [112] Kaiyu Yang, Klint Qinami, Li Fei-Fei, Jia Deng, and Olga Russakovsky. Towards fairer datasets: filtering and balancing the distribution of the people subtree in the imagenet hierarchy. In Mireille Hildebrandt, Carlos Castillo, L. Elisa Celis, Salvatore Ruggieri, Linnet Taylor, and Gabriela Zanfir-Fortuna, editors, *FAT* '20: Conference on Fairness, Accountability, and Transparency, Barcelona, Spain, January 27-30, 2020*, pages 547–558. ACM, 2020. 8
- [113] Lior Yariv, Jiatao Gu, Yoni Kasten, and Yaron Lipman. Volume rendering of neural implicit surfaces. *arXiv preprint arXiv:2106.12052*, 2021. 9
- [114] Alex Yu, Vickie Ye, Matthew Tancik, and Angjoo Kanazawa. pixelnerf: Neural radiance fields from one or few images. In *Proc. CVPR*, pages 4578–4587, 2021. 10, 11, 15, 16
- [115] Greg Zaal, Rob Tuytel, Rico Cilliers, James Ray Cock, Andreas Mischok, Sergej Majboroda, Dimitrios Savva, and Jurita Burger. Polyhaven: a curated public asset library for visual effects artists and game designers, 2021. 5, 10
- [116] Yuxuan Zhang, Huan Ling, Jun Gao, Kangxue Yin, Jean-Francois Lafleche, Adela Barriuso, Antonio Torralba, and Sanja Fidler. Datasetgan: Efficient labeled data factory with minimal human effort. In *CVPR*, 2021. 2
- [117] Jia-Xing Zhao, Jiang-Jiang Liu, Deng-Ping Fan, Yang Cao, Jufeng Yang, and Ming-Ming Cheng. Egnnet: Edge guidance network for salient object detection. In *Proceedings of the IEEE/CVF International Conference on Computer Vision*, pages 8779–8788, 2019. 9
- [118] Shuaifeng Zhi, Tristan Laidlow, Stefan Leutenegger, and Andrew J. Davison. In-place scene labelling and understanding with implicit scene representation, 2021. 2
- [119] Xingyi Zhou, Dequan Wang, and Philipp Krähenbühl. Objects as points. *arXiv preprint arXiv:1904.07850*, 2019. 8
- [120] Tyler Zhu, Per Karlsson, and Christoph Bregler. Simpose: Effectively learning densepose and surface normals of people from simulated data. In *European Conference on Computer Vision*, pages 225–242. Springer, 2020. 8